TET1-mediated Oligodendrocyte Homeostasis Regulates Myelination and Synaptic Functions

Ming Zhang[1,6], Jian Wang[1,6], Kaixiang Zhang[1,6], Guozhen Lu[1], Lingli Xu[2], Keke Ren[1], Wenting Wang[1], Yuming Liu[1], Junlin Xing[1], Xingchun Gao[3], Weilin Jin[4], Kalen Berry[2], Hehuang Xie[5], Shengxi Wu[1], Q. Richard Lu[2, *] and Xianghui Zhao[1,3,7,*]

[1] Department of Neurobiology and Collaborative Innovation Center for Brain Science, School of Basic Medicine, Fourth Medical University, Xi'an, Shaanxi 710032, China

[2] Division of Experimental Hematology and Cancer Biology, Department of Pediatrics, Cincinnati Children's Hospital Medical Center, Cincinnati, OH 45229, USA

[3] Shaanxi Key Laboratory of Brain Disorders, Xi'an, Shaanxi 710021 China

[4] School of Electronic, Information and Electrical Engineering, Shanghai Jiao Tong University, Shanghai 200240, China

[5] School of Neuroscience & Department of Biological Sciences, Virginia Tech, Blacksburg, VA 24061, USA

[6] These authors contributed equally to this work.

[7] Lead contact

Running title: TET1 Epigenetic control of CNS Myelination

*Corresponding authors

To Xianghui Zhao, School of Basic Medicine, Fourth Medical University, Xi'an, Shaanxi 710032, China. Email: xianghuizhao@fmmu.edu.cn; or Q. Richard Lu, Department of Pediatrics, Cincinnati Children's Hospital Medical Center, Cincinnati, OH, USA. Email: richard.Lu@cchmc.org.

Abstract

DNA methylation is critical for oligodendrocyte development. The role of the converse process, DNA demethylation regulated by Ten-Eleven-Translocation (TET) dioxygenases, in oligodendrocyte homeostasis, myelination and remyelination however remains elusive. Here, we identify a genome-wide and locus-specific DNA hydroxymethylation landscape shift during oligodendrocyte progenitor cell (OPC) differentiation. *Tet1* ablation results in defects in oligodendrocyte development and myelination in the developing brain, while impairing remyelination after demyelination in adult brains. Transcriptomic and DNA hydroxymethylation analyses reveal a TET1-regulated epigenetic program for oligodendrocyte differentiation and identify a set of target genes associated with Ca^{2+} homeostasis. *Tet1*-deficient OPCs exhibited reduced [Ca^{2+}] oscillations, while activation of calcium channels partially restores the differentiation defect of *Tet1*-deficient OPCs. Moreover, dysregulated oligodendrocyte homeostasis caused by *Tet1*-deficiency impairs action potential propagation and synaptic transmission. Thus, our results suggest that stage-specific TET1-mediated epigenetic programming of oligodendrocyte homeostasis is required for proper myelination and repair as well as neuronal physiology in cell-autonomous and non-cell-autonomous mechanisms, respectively.

Keywords: DNA demethylation, hydroxymethylation, TET dioxygenases, epigenetics, oligodendrocyte, differentiation, calcium homeostasis, neuronal activity

Introduction

Myelination by oligodendrocytes (OLs) enables saltatory conduction of action potentials and provides long-term trophic support for axons, maintaining integrity throughout the central nervous system (CNS) (Nave and Werner, 2014). The formation of mature myelinating OLs is a complex process that is tightly coordinated by genetic and epigenetic events in a spatially and temporally specific manner (Emery and Lu, 2015; Zuchero and Barres, 2013). Epigenetic regulation such as DNA methylation, histone modifications, and chromatin remodeling are critical for multiple aspects of OL development, function and regeneration (Gregath and Lu, 2018; Liu et al., 2016; Lu et al., 2019). For instance, proper maintenance of genomic cytosine methylation (5mC) is essential for the normal development, homeostasis, and function of mammalian cells (Iurlaro et al., 2017; Smith and Meissner, 2013). Genetic ablation of DNA methyltransferases 1 (DNMT1), which maintains DNA methylation after replication, resulted in impaired OL precursor cell (OPC) expansion and differentiation during early development (Moyon et al., 2016). In adults, the role of DNMT1 appears diminished as reduction in *Dnmt3a* expression, but not *Dnmt1*, leads to defective OPC differentiation and remyelination after injury (Moyon et al., 2017).

Although DNA methylation in terminally differentiated cells was largely irreversible, the modified nucleotide 5-hydroxymethylcytosine (5hmC) was recently discovered as an intermediate product generated during cytosine demethylation (Kriaucionis and Heintz, 2009; Tahiliani et al., 2009). DNA demethylation like methylation is a highly regulated process mediated by specialized enzymes, the Ten-Eleven Translocation (TET) family of dioxygenases. TET enzymes oxidize 5mC into 5hmC and initiate the active DNA demethylation process (Ito et al., 2010; Tahiliani et al., 2009). Dynamic cytosine methylation or demethylation has been established as common epigenetic modification regulating various processes from development to diseases in a cell-type and context-dependent manner (Graff et al., 2011; Sun et al., 2014; Szulwach et al., 2011b). Although TET enzymes are present in OL lineage cells (Zhao et al., 2014), at present, whether and how DNA demethylation contribute to OL lineage development, myelination and remyelination after injury remain poorly defined.

In this study, we demonstrate a genome-wide shift in 5hmC landscape during OL specification and identify an age-dependent function of TET1 in OL lineage development and homeostasis. A TET1-regulated epigenetic program is also required for efficient remyelination as depletion of *Tet1* in adult animals impaires recovery after demyelinating injury. *Tet1* depletion results in genome-wide alterations in 5hmC and transcriptome profiles in OPCs. One pathway that is disproportionally altered in this process is a set of calcium transporter genes, such as $Ca_v1.2$, $Ca_v2.1$ and *Itpr2*. Our results further show that TET1-mediated Ca^{2+} homeostasis is critical for OL differentiation in vitro. Strikingly, we find that *Tet1* depletion in OL lineage cells leads to reduced expression of secreted factors such

as GDNF (glial cell line derived neurotrophic factor) and an impairment of synaptic transmission. These data suggest that TET1 regulates normal OL lineage differentiation, proper oligodendrocyte-neuron communication and neuronal activities by both cell-autonomous and cell non-autonomous signaling pathways.

Results

DNA hydroxymethylation landscape dynamics during OL lineage differentiation

To investigate the 5hmC landscape marking DNA demethylation during the OL lineage transition, we carried out antibody-based 5hmC immunoprecipitation combined with Illumina sequencing (hMeDIP-seq) (Ficz et al., 2011; Xu et al., 2011) to analyze the 5hmC distribution across the genome. We compared 5hmC distribution within OPCs to those in neural progenitor cells (NPCs) (Li et al., 2017) and identified 1237 genes that were specifically hydroxymethylated in the promoter-TSS region of OPCs but not in NPCs (Figure 1A). Gene ontology (GO) analysis identified gene terms that are highly associated with OPC differentiation, such as cell projection organization, fatty acid transport, regulation of cytosolic calcium ion concentration, as well as signaling pathways that are essential for OL development, such as the G-protein coupled receptor pathway (Chen et al., 2009; Mogha et al., 2016) (Figure 1B). Further comparisons with a neural cell-type transcriptome dataset (Zhang et al., 2014) revealed a significant increase in the 5hmC signal among OL-associated gene loci during OPC differentiation, including *Cspg4* (chondroitin sulfate proteoglycan 4), *Mag* (myelin-associated glycoprotein) and *Elovl7* (elongation of very long chain fatty acids protein 7) (Figure 1C and Figure S1). In contrast, the genes with 5hmC peaks enriched in promoter-TSS regions from NPCs were associated with negative regulation of OL differentiation including *Id2, Ngf and Zfp28* (Figure 1D). These data suggested a unique distribution pattern of genomic 5hmCs in the gene loci associated with OL lineage progression during the transition of OPCs from NPCs.

Deletion of *Tet1* in OL lineage causes myelination deficits at early postnatal stages

Given that DNA hydroxymethylation is catalyzed by the TET family of dioxygenases and that TET enzymes are present in OL lineage cells (Zhao et al., 2014), we assessed the function of TET family enzymes TET1 and TET3 in OL development since TET2 had no detectable effects in OL lineage development (personal communication with Dr. P. Casaccia). We crossed the *Tet1*$^{f/f}$ (Zhang et al., 2013) and *Tet3*$^{f/f}$ (Gu et al., 2011) mice with *Olig1-Cre* line (Xin et al., 2005) to knockout the catalytic domains of these TETs early in the OL lineage (Figure 1E and Figure S2A). The resulting *Tet1*$^{flox/flox}$;*Olig1*Cre$^{+/-}$ (*Tet1* cKO) and *Tet3*$^{flox/flox}$;*Olig1*Cre$^{+/-}$ (*Tet3* cKO) mice were born at Mendelian ratios and appeared normal at birth.

We did not detect significant differences in either the number of mature OLs or myelin protein

expression between heterozygous *Tet1* floxed mice (*Tet1*$^{flox/+}$;*Olig1*Cre$^{+/-}$), *Cre* control (*Tet1*$^{+/+}$;*Olig1*Cre$^{+/-}$), or wild-type mice (Figure S3), heterozygous littermates were then used as controls. To assess Cre-mediated *Tet1* depletion, we compared *Tet1* expression between groups in OPCs, which have been previously demonstrated to have the highest *Tet1* levels during OL differentiation (Zhao et al., 2014). Immunostaining and quantitative real-time PCR revealed decreased expression of TET1 in the corpus callosum at P4 (Figure 1F-G) and in purified OPC cultures (Figure 1H).

To investigate the effects of TET1 on OL development, we examined the expression of SOX10 (an OL lineage marker), and mature OL markers CC1 and MBP (myelin basic protein). The number of CC1$^+$ mature OLs was significantly reduced in juvenile *Tet1* cKO mice (Figure 1I-J), but these developmental defects were no longer apparent in adult mutants (Figure 1J and Figure S4A). Expression of MBP was also substantially decreased in both cortex (gray matter) and corpus callosum (white matter) from P16 *Tet1* cKO mice (Figure 1K), but was recovered to control levels in older animals (Figure S4A-B). Additionally, the purified oligodendrocyte precursor cells from *Tet1* cKO mice showed prominently decreased numbers of CNPase- or MBP-positive cells during differentiation compared to control (Figure 2A-B). Together, these observations indicate that *Tet1* loss causes a significant delay in OL maturation both *in vivo* and *in vitro*. In contrast, the same experiments in the *Tet3* cKO animals did not show any significant differences between mutants and controls (Figure S2). Therefore, we focused our efforts onto examining the processes underlying the observed myelination defects in *Tet1* cKO mice.

The ultrastructure observation of optic nerve by electron microscopy (EM) revealed that the number of myelinated axons was significantly reduced in *Tet1* mutants (Figure 2C-D), and a few myelinated axons in *Tet1* cKO optic nerves were characterized by higher G ratio and thinner myelin sheaths (Figure 2C, E). The myelination deficits were further examined in the corpus callosum from *Tet1* cKO mice at P14 and P27 (Figure 2F-J). However, the myelin ultrastructure defects were no longer identifiable in two-month old adult *Tet1* cKO animals (Figure 2F, K-L). Notably, this myelin defect was not recapitulated in spinal cord. Although the numbers of CC1$^+$ mature OLs were slightly decreased in mutant spinal cord at P8 (Figure S5A-C), we did not detect a substantial alteration in MBP expression at this age (Figure S5D). In addition, similar ultrastructure of myelin was detected under EM at P14 (Figure S5E-F). These observations suggest a stage-dependent and region-specific function of TET1 in CNS myelination.

Given the recovery seen in adults from the earlier developmental defects in myelination, we asked whether this recovery was due to the compensation from cells that escaped Cre mediated recombination. In adulthood, TET1 expression in OLs was low (Figure S4C) as previously reported (Zhao et al., 2014), but the percentage of TET1$^+$/Sox10$^+$ OL lineage cells reached ~80% in *Tet1* cKO

mice (Figure S4C-D). These results suggest that the adult OLs expressing TET1 may escape from Cre-mediated *Tet1* depletion and compensate for the myelin deficiency earlier in the *Tet1* cKO animals.

To evaluate the neurological significance of hypomyelination in *Tet1* cKO mice, we analyzed stimulus-evoked compound action potential (CAP) in optic nerves (Devaux et al., 2002; Devaux and Gow, 2008; Stys et al., 1991). Suction electrodes back filled with artificial cerebrospinal fluid (aCSF) were used for stimulation and recording. In P14 optic nerves, both the peak amplitude and the CAP area, which are indexes of excited myelinated axon numbers and nerve function (Devaux et al., 2002; Devaux and Gow, 2008), showed significant reduction under different stimulating currents in *Tet1* cKO mutants (Figure S6), indicating a defective nerve conduction in *Tet1* cKO mutant optic nerves in line with the ultrastructural studies showing defects in myelination.

Ablation of *Tet1* results in defects in OPC cell cycle progression

Concomitant with the myelin deficiency, we observed a marked reduction of Olig2-positive cells from the embryonic stage in *Tet1* cKO animals at E15.5 (Figure S4E-F). Moreover, the number of platelet-derived growth factor receptor α (PDGFRα)$^+$ cells in the mutant cortex was reduced to ~63% compared to the controls in P1 mutant, suggesting a downsized OPC pool (Figure 3A-B).

To determine the underlying defects leading to a reduction in the OPC and OL population in *Tet1* juvenile mutants, we first tested the possibility of apoptosis in OPCs with the TUNEL assay. Combined with Olig2 staining, brain sections from E14.5, E17.5 and P1 mice revealed no distinguishable changes in the number of TUNEL$^+$ apoptotic cells among Olig2$^+$ OL lineage cells between *Tet1* cKO animals and control littermates (Figure S7A-B).

Next, a BrdU incorporation assay was performed to examine the proliferation of OPCs. *Tet1* cKO mice at P1 were pulse-chased with BrdU and sacrificed 2 hours later. Compared to controls, the percentage of BrdU and Sox10 double-positive cells in the OL lineage showed a slight but significant increase in the *Tet1* cKO cortex (Figure 3C-D). Similar results were also observed with another cell proliferation marker Ki67 (Figure S7C-D). In addition, we validated the proliferation changes in purified OPC cultures. Both Ki67 and BrdU staining showed increased proliferating numbers of OPCs from *Tet1* mutants (Figure 3E-G).

To further investigate the stage of cell cycle blockage in *Tet1*-deficient OPCs, we performed flow cytometry with propidium iodide (PI) DNA staining in purified OPCs. A significant increase in the percentage of cells in S phase (23.21 % ± 3.12) and G2/M phase (13.83 % ± 1.91) was observed in OPCs from *Tet1* mutants compared to the controls (11.84% ± 2.46 for S phase and 7.09 % ± 1.17 for G2/M phase), and there was a concomitant reduction in the number of cells in G1 phase in *Tet1* mutants (Figure 3H-I). These results suggested that the proliferation of OPCs from *Tet1* cKO brain

might be blocked at the transition from G2/M to G1 phase, which could impair OPC cell cycle progression, leading to a reduction in OPC numbers.

In addition, we noted that *Tet1* deletion did not appear to substantially alter the number of other neural cell types in the brain. Western blot and immunostaining with antibodies against DCX, a marker for newly generated neurons, NeuN, a mature neuron marker, and ALDHL1, an astrocyte marker, revealed that there was comparable neuron and astrocyte pools between controls and *Tet1* mutants (Figure S8). Taken together, our data suggest that the abnormal cell cycle progression of OPCs and delayed OPC differentiation may contribute to the reduced OL numbers and hypomyelination in *Tet1*-deficient juvenile mice.

Ablation of *Tet1* impairs adult remyelination after demyelination

Given the critical role of TET1 in early oligodendrocyte development, we hypothesized that TET1 is also required for remyelination after demyelination in the adult brain. We induced demyelinated lesions in the corpus callosum via stereotaxic guided lysolecithin (LPC) injections (Figure 4A). LPC induces rapid myelin breakdown followed by myelin regeneration through an OPC recruitment phase at 7 days post-lesion (7 dpl) and a remyelination phase at 14 dpl *in vivo*. TET1$^+$ cell numbers were increased substantially in the lesion site at 7 dpl relative to vehicle controls (Figure 4B-C). In particular, the expression levels of TET1 in Olig2$^+$ cells appeared much more robust after LPC treatment (Figure 4B-C).

To determine the potential role of TET1 in remyelination, we bred *Tet1*$^{flox/flox}$ mice with *NG2-CreER*^{T} (Zhu et al., 2011), an OPC-specific tamoxifen-inducible Cre line to generate *Tet1* OPC-iKO (*NG2-CreER*^{T}:*Tet1*$^{flox/flox}$) animals. In the *Tet1* OPC-iKO mice, which were treated with tamoxifen injection from P2-P5 daily, we observed a reduction in CC1$^+$ and MBP$^+$ OLs at P7 and P14 (Figure S9). To induce recombination in adult mice, 8-week-old *Tet1* OPC-iKO mice were injected daily with tamoxifen for 8 days, starting 3 days prior to LPC injection in the corpus callosum (Figure 4D). Heterozygous littermates (*NG2-CreER*^{T}:*Tet1*$^{flox/+}$) served as controls. Brains were harvested at 7, 14 and 21 dpl. To determine the extent of remyelination, we examined the expression of OPC markers and myelin related genes. Loss of *Tet1* did not appear to impair the recruitment of PDGFRα$^+$ OPCs and the number of OPCs in the lesion was comparable between control and *Tet1* OPC-iKO mice during the recruitment phase at dpl 7 (Figure 4E-F). In contrast, there were significantly fewer GST-pi$^+$ differentiating OLs in the lesion site during the remyelination phase at dpl 14 and dpl 21 relative to control (Figure 4E, G). Consistent with a reduction in the number of differentiating OLs, MBP was also reduced in *Tet1*-iKO lesions compared to control at dpl 21 (Figure 4H). Notably, far fewer remyelinated axons were detected in the lesions of *Tet1*-iKO mice than controls at dpl 21 (Figure 4I-J). The percentage of myelinating axons and the thickness of newly generated myelin sheaths

around axons assessed by g-ratios were significantly reduced in *Tet1*-iKO mutants (Figure 4J-K). These observations indicate that TET1 is required for the proper remyelination in the context of white matter injury.

Transcriptome alterations and a genome-wide decrease of 5hmC in *Tet1*-ablated OPCs

To investigate the molecular underpinnings of the observed defects in early oligodendrocyte development, we compared the RNA transcriptome in purified OPC cultures from control and *Tet1* cKO neonates (Figures 5A). There were approximately 1880 genes downregulated and 881 genes upregulated in *Tet1* mutants compared with controls (FDR<0.05, Log_2>1 or <-1) (Table S1), suggesting that the predominant effect of *Tet1* loss was transcriptional repression. Consistent with the abnormal cell cycle and deficient myelin formation in *Tet1* mutants, gene set enrichment analysis (GSEA) indicated that myelination and cell cycle regulation gene sets in *Tet1*-ablated OPCs were downregulated (Figures 5B, E, G), including genes related to the G2-M cell cycle, cell division, OL differentiation and ensheathment of axons. In contrast, gene ontology (GO) terms associated with the mitochondria gene module and immune-related functions were upregulated in *Tet1* cKO OPCs (Figure 5B-C). Quantitative PCR confirmed representative gene expression changes associated with these gene set enrichments in the RNA-seq data (Figure 5D, F, H). Indeed, OL differentiation and myelination-associated genes, such as *Mbp*, *Plp1*, *Myrf*, *Enpp2*, *Cnp*, *Cldn11*, *Ugt8a*, *Kif11*, and *Bcas1* were markedly downregulated in *Tet1* cKO OPCs as well as multiple genes involved in cell cycle regulation. The transcriptome landscape alterations in *Tet1* cKO OPCs were in line with the observations that *Tet1* depletion led to cell cycle progression defects and hypomyelination phenotypes.

Since TET1 mediates DNA hydroxymethylation/demethylation, we next tested the level of 5hmC in oligodendrocytes from *Tet1* mutants. In P27 brain sections, immunostaining of 5hmC along with OL marker CC1, revealed a striking reduction in 5hmC intensity in oligodendrocytes (Figure 6A-B), which strongly suggested that 5hmC is involved in TET1-regulated OL differentiation.

To further compare the genome-wide 5hmC distribution changes, we performed hMeDIP-seq in OPC cultures from controls and *Tet1* mutants. *Tet1* cKO OPCs showed a dramatic reduction in 5hmC peak signals compared to controls (Figure S10A), which was consistent with the immunostaining results. In both groups, most 5hmC peaks resided in the intergenic region, and less than 40% of peaks were found to be within the gene bodies of annotated RefSeq genes (Figure S10B), which is different from the distribution pattern in mouse embryonic stem cells (Xu et al., 2011) and neurons (Hahn et al., 2013). After plotting the distribution of 5hmC peaks over RefSeq genes, we found that 5hmC was reduced near the transcription start site (TSS) and transcription terminal site (TTS) in control OPCs, and *Tet1* depletion caused a global reduction of 5hmC, especially at the intragenic

region, promoter, and TTS (Figure 6C and Figure S10B). For the 5hmC peak distribution around TSS (5-kb upstream and downstream of TSS), heatmap clustering revealed that there were five distributed groups, and there was an overall decrease in the level among all five groups in *Tet1* cKO samples (Figure 6D). Further analysis showed that most differentially hydroxymethylated regions (DhMRs) between the *Tet1* cKO and control groups were associated with low CpG density, which was less than 1 CpG per 100 bp (Figure S10C).

We next examined the effects of TET1 mediated DNA hydroxymethylome on gene expression. By integrating RNA-seq data with hMeDIP-seq data, we observed that among the decreased lower hydroxymethylated gene peaks in gene body regions from *Tet1* cKO mice, 12.83% genes expression were downregulated (1026 of 7998) and 4.89% genes were upregulated (391 of 7998) (Figure 6E). The correlation percentage is comparable to DhMRs in promoter regions, 13.46% and 6.42% in downregulated and upregulated genes, respectively (Figure S10D-E). Therefore, these observations indicated that DNA hydroxymethylation is positively correlated to gene expression.

Among the genes that showed both downregulated mRNA expression and decreased gene body 5hmC levels in *Tet1* cKO mice, many are associated with myelination, cell division and calcium transportation (Figure 6F-G). For example, *Mbp*, *Mobp*, and *Cnp* are myelin genes. *Tcf7L2*, *Myrf*, and *Enpp2/6* are involved in the regulation of OL differentiation in a stage-specific manner within different transcriptional circuitry (Hornig et al., 2013; Morita et al., 2016).

When searching for TET1-5hmc regulated factors that may involve in OL development and homeostasis, we noticed that there was a cluster of calcium transporter genes among the downregulated genes in *Tet1* cKO group, which can be further confirmed by qRT-PCR assays (Figures 5I-J). CACNA1a, CACNA1c, CACNA2d1, CACNB4, and CACNG5 are all well-known plasma membrane voltage-operated Ca^{2+} channels (VOCCs) that are expressed in OPCs and contribute to Ca^{2+} dynamics in these cells (Larson et al., 2016; Zhang et al., 2014). In particular, Ca^{2+} influx mediated by CACNA1c, also known as $Ca_V1.2$, is required for oligodendrocyte differentiation (Cheli et al., 2016; Cheli et al., 2015). Another gene *Itpr2*, which encodes an endoplasmic reticulum (ER) localized type 2 IP_3 receptor (IP_3R2), a specific Ca^{2+} channel in postmitotic OLs (Zeisel et al., 2015), also showed decreased mRNA expression in OPCs from *Tet1* cKO mice (Figure 5J). In addition, a set of the genes encoding secreted factors (e.g. GDNF) and extracellular matrix proteins (e.g. Tenascin-R and Reelin), were also significantly decreased in *Tet1* cKO OPCs (Figure 5K-L). Especially, the level of GDNF from both the cell extraction and supernatant of OPC cultures were significantly reduced in *Tet1* cKO mice (Figure S11A-B). These observations indicated that TET1-5hmc regulates calcium homeostasis in OL lineage cells and the secretion of regulators of neuronal development for the intracellular communication between OPCs and their neighbors.

Impaired Ca^{2+} dynamics in *Tet1* cKO leads to OPC differentiation defects

Calcium signaling and homeostasis have been shown to be important for OPC migration, differentiation and initiation of myelin formation (Butt, 2006; Friess et al., 2016; Li et al., 2018; Zhang et al., 2019). The downregulation of multiple calcium transporter genes in OPCs from *Tet1* cKO mice prompt us to test the $[Ca^{2+}]_i$ oscillations in culture. A Fluo4-based Ca^{2+}-imaging approach was employed to compare the influx of Ca^{2+} between groups in combination with Bay K 8644, a L-type calcium channel agonist (Greenberg et al., 1984), or verapamil, an inhibitor of L-type voltage operated Ca^{2+} channels (VOCCs) (Cheli et al., 2015). In OPC cultures, we noticed that bath application of Bay K 8644 (10 μM) induced a transient and synchronous increase of $[Ca^{2+}]_i$ in the control groups (Figure 7A-B, Supplementary Movie 1). In *Tet1* cKO group, a lower amplitude 3.649±0.1218 AU in control and 3.102±0.1874 AU in mutant) and slower kinetics for onset (0.8589±0.03827 in control and 0.6759±0.03634 in mutant) were observed after application of Bay K 8644 (Figure 7A-D, Supplementary Movie2). Importantly, the increase in intracellular Ca^{2+} in *Tet1* cKO OPCs was blocked by the specific L-VOCC inhibitor, verapamil (5 μM) (Figure 7B). These results indicated that ablation of *Tet1* could greatly reduce VOCC mediated Ca^{2+} influx in OPCs.

To confirm, we tested the effects of another trigger for Ca^{2+} entry, adenosine triphosphate (ATP), on $[Ca^{2+}]_i$ oscillations in OPCs. ATP can mobilize Ca^{2+} from intracellular ER stores or trigger Ca^{2+} influx across the plasma membrane (Kirischuk et al., 1995; Stevens et al., 2002). Similar to the results of Bay K 8644 application, the amplitude of 100 μM ATP-induced $[Ca^{2+}]_i$ transients was significantly higher in control cultures (7.061±0.2118 AU) than in the *Tet1* mutant cultures (4.417±0.1649 AU, Figure 7E-F), and the kinetics of onset were slower in the mutants as well (3.647±0.2791 in control and 2.968±0.1595 in mutant, Figure 7G). Since ATP evokes large and prolonged increases in $[Ca^{2+}]_i$ from intracellular stores mainly via P2Y purinoceptors, especially P2Y1 in OL (Agresti et al., 2005; Kirischuk et al., 1995), we applied a specific antagonist for the P2Y1 receptor, MRS2179 (100 μM), prior to ATP stimulation. In the presence of MRS2179, the $[Ca^{2+}]_i$ response was significantly repressed in both groups (Figure 7E), which is consistent with the findings of other study (Agresti et al., 2005), and indicated that ATP-induced $[Ca^{2+}]_i$ oscillations in OPCs are mainly attributable to an action on P2Y1 receptors. These results suggested that the reduced expression of calcium transporters on both the cell membrane and the ER membrane in *Tet1* cKO group is responsible for the reduced $[Ca^{2+}]_i$ oscillations in OPCs from *Tet1* cKO mice.

As for the consequences of $[Ca^{2+}]_i$ oscillation changes in *Tet1* cKO OPCs, we further examined the effects of calcium channel agonist Bay K 8644 on the differentiation and proliferation of OPCs. Consistent with the results of high K^+ application (Cheli et al., 2015), daily three consecutive pulses (5min/each) of Bay K 8644 (10 μM) in OPC cultures significantly promoted OPC differentiation by increasing the expression of myelin genes (Figure 7H-J). Importantly, Bay K 8644 treatment

significantly restored the differentiation defects in *Tet1* cKO OPC cultures, as determined by qRT-PCR analysis of myelin genes and MBP^+ OL formation (Figure 7H-J). In addition, Bay K 8644 application significantly reduced OPC proliferation and the percentage of cells in S phase assayed by BrdU incorporation (Figure 7K-L) and flow cytometry (Figure S11C-E), respectively. These data indicate that TET1 modulated $[Ca^{2+}]_i$ oscillation plays an important role in the OL differentiation process.

Synaptic dysfunctions in the *Tet1* cKO brain

Insufficient or abnormal myelination has been reported to disrupt synaptogenesis and synaptic transmission in addition to the expected defects in nerve conduction associated with reduced membrane capacitance (Wang et al., 2018). Meanwhile, growth factors and extracellular matrix components, such as GDNF (Ledda et al., 2007), Tenascin-R (Ferrer-Ferrer and Dityatev, 2018), and Reelin (Ventruti et al., 2011; Wasser and Herz, 2017), are also critical for shaping and strengthening neuronal synapses. We therefore determined whether the epigenetic alterations due to *Tet1* ablation in OL lineage cells can affect synaptic density and strength in a non-cell autonomous manner.

We compared spontaneous excitatory postsynaptic currents (sEPSCs) and miniature excitatory postsynaptic currents (mEPSCs) from pyramidal excitatory neurons in M2 cortex of P21~P22 mice. For sEPSCs, there is a chance of action potential-driven events due to intrinsic properties of presynaptic cell or network activity. All the mEPSCs, in turn, were recorded in the presence of TTX, which blocks action potential generation and propagation via blockage of TTX-sensitive sodium channels. Thus, mEPSCs are spontaneous in the sense of not being evoked by action potentials sensitive to the myelination status of axons, but rather reflect intrinsic synaptic properties (Pinheiro and Mulle, 2008). We found that the frequency of both sEPSCs and mEPSCs were significantly decreased in *Tet1* cKO neurons (Figure 8A-B, D-E), but the amplitude was comparable between groups for either sEPSCs or mEPSCs (Figure 8C, F). These observations suggest *Tet1*-deletion in the OL lineage leads to either a decrease in synaptic density or alterations in presynaptic strength.

To determine what processes may underly the defects in sEPSC or mEPSC frequency, we first performed electron microscopy to look for alterations in synapse numbers. The ultrastructural analysis indicated that synaptic density in P21 M2 cortex was similar between both groups (Figure S12A-B). To further examine potential alterations on the presynaptic side, we analyzed the density of puncta positive for the presynaptic marker synaptophysin and the excitatory presynaptic terminal markers vesicular glutamate transporter 1 (vGlut1) and 2 (vGlut2). These markers were significantly decreased in M2 cortex of P21 *Tet1* cKO brain (Figures 8G-H and Figure S12C). However, the number of puncta displaying the postsynaptic marker Homer1 did not obviously different between groups (Figures 8H and Figure S12C). Immunoblotting for the pre- and post-synaptic markers was

consistent to the histological results (Figure 8I-J), suggesting a downregulation of presynaptic protein expression in the *Tet1* cKO cortex. Therefore, our results indicate that the loss of TET1 in oligodendrocyte lineage cells can cause a disruption of pre-synaptic strength without altering the number of synapses in neurons.

Discussion

Stage-specific TET1 functions in OL development and remyelination

DNA methylation, which mainly deposits 5mC mark on CpG islands in the genome, enables stable but reversible transcription repression and is critical for mammalian development (Iurlaro et al., 2017; Smith and Meissner, 2013). Defects in the regulation of DNA methylation have been associated with various neurological diseases (Gopalakrishnan et al., 2008; Lu et al., 2013). TET enzymes reverse the methylation actions of DNMTs through oxidizing 5mC into 5hmC and promote DNA demethylation (Ito et al., 2010; Kriaucionis and Heintz, 2009; Tahiliani et al., 2009). Strikingly, we detected a genome-wide change in the DNA demethylation landscape marked by 5hmC during OPC differentiation from neural progenitor cells, suggesting a role of TET-mediated DNA demethylation in regulation of OL lineage progression.

In the present study, we found that TET1, but not TET2 or TET3 (Figure S2, and personal communication with Dr. P. Casaccia), is critical for OPC proliferation, differentiation and myelination during early animal development, suggesting a unique function of TET1 among the TET family in oligodendrogenesis and subsequent myelinogenesis during development. In contrast to early developmental defects, we found that the developmental myelin deficiencies recovered in adult *Tet1* cKO mice. We noticed that the percentage of TET1 and Sox10 double positive cells recovered to ~80% in adult *Tet1* cKO mice, therefore we speculate that these OLs escaped from Cre-mediated *Tet1* depletion in OPCs stage may gradually expand and replace the mutant cells in later stage to some extent. Additionally, the remyelination capacity after injury was compromised in mature *Tet1* OPC-iKO brains, indicating that TET1 remains critical for the myelin regeneration process. Similar results were observed by Dr. P. Casaccia and colleagues using another *Tet1*$^{f/f}$ line (personal communication), indicating a stage-dependent function of TET1 in OL myelination and remyelination.

Although the OL differentiation defect was not due to increased apoptosis in the *Tet1* cKO mutant brain, we found that OPC cell cycle progression was impaired in *Tet1* cKO animals. TET1 has been implicated in regulation of cell-cycle progression. For instance, TET1 is critical to maintain the stability of cyclin B1 and acts as a facilitator of mitotic cell-cycle progression (Chrysanthou et al., 2018; Huang et al., 2013). In line with these studies, we found that a cluster of 5hmC-enriched cell cycle genes, e.g. *Ccng2*, *Cdca3, Ccna2*, *Ccnb2* and *Cdc25b* (Bennin et al., 2002; Boutros et al., 2013; Kalaszczynska et al., 2009; Nagi Ayad, 2003; Timofeev et al., 2010), were down-regulated in

the *Tet1* cKO OPCs, suggesting that TET1-5hmC is also critical for cell cycle progression in OPCs.

Locus-specific alteration of DNA hydroxymethylation landscape in OPCs from *Tet1* mutants

Genome-wide mapping of 5hmC from *Tet1* cKO animals indicated that TET1 is required for maintaining the proper level of 5hmC in a locus-specific manner during OL differentiation. Despite variable in the promoter regions (Shi et al., 2017), 5hmC signals have been associated with gene transcription and localized in the gene bodies of actively regulated genes in ESCs and NPCs (Stroud et al., 2011; Tan et al., 2013; Xu et al., 2011). For example, in gene bodies, 5hmC peaks are positively correlated with gene expression levels in ESCs (Xu et al., 2011), but show lower levels in NPCs (Tan et al., 2013). The analysis of the differentially hydroxymethylated genes along with transcriptome profile changes indicates that 5hmC signals in gene bodies are more preferentially associated with gene expression changes than those in promoter regions in OPCs. This suggests that 5hmC modification by TET1 regulates locus-specific gene expression programs for OPC differentiation.

On the other hand, 5hmC may regulate gene expression through associations with various regulatory elements and processes (Szulwach et al., 2011a; Szulwach et al., 2011b), including histone modification and chromatin configuration at the specific loci during cell growth and differentiation. For example, in ES cells, 5hmC is accumulated at the “bivalent domains” in promoters or enhancers that are decorated with dual histone markers, e.g. activating (H3K4me3) and repressive (H3K27me3), for gene transcription (Bernstein et al., 2006; Pastor et al., 2011). Whether and how 5hmCs cooperate with other epigenetic regulators for OPC differentiation remain to be determined.

Intriguingly, ablation of *Tet1* also led to upregulation of a set of genes in OPCs, indicating that TET1-mediated 5hmC deposition may also function as a transcription repressor. Consistently, knockdown of *Tet1* has been shown to increase a set of targeted genes in ESCs (Williams et al., 2011; Wu et al., 2011). TET1-mediated repression might involve in a recruitment of the MBD3/NuRD repressor complex, which was shown to co-localize with TET1 in ESCs (Yildirim et al., 2011). TET1 may also coordinate with Sin3A co-repressor complex, which has a similar binding profile to TET1 and is required for a subset of TET1-repressed target genes (Neri et al., 2013; Williams et al., 2011). A recent study indicates that TET1 mediated transcriptional repression could channel through JMJD8 demethylase transcriptional repressor and is independent of TET1 catalytic activity during epiblast differentiation (Khoueiry et al., 2017). Therefore, the mechanisms of locus-specific transcriptional regulation by TET1 during OL development remain to be further defined.

TET1-mediated Ca^{2+} homeostasis is critical for oligodendrocyte differentiation

“Calcium signaling” is critical for the response of glial cells to multiple extracellular stimuli. For

instance, blocking of the voltage-operated Ca^{2+} entry in OPCs inhibits their maturation and the myelin formation ability (Cheli et al., 2015). Similarly, an increase of the resting intracellular [Ca^{2+}] through membrane depolarization could facilitate MBP synthesis in OPCs (Friess et al., 2016).

We found that *Tet1* deletion led to the downregulation of multiple calcium transporter genes in OPCs. Treatment of calcium channel agonist significantly restored the differentiation defects in *Tet1*-dificient OPCs. Ca^{2+} transients in OLs have been shown to regulate retraction and elongation of the developing myelin sheath (Baraban et al., 2018; Krasnow et al., 2018). Our data indicated that the $[Ca^{2+}]_i$ oscillations from both extracellular influx and intracellular stores were greatly reduced in OPCs isolated from *Tet1* cKO mice, and that inhibition of VOCC activation impaired OPC differentiation. These observations suggest that TET1-regulated calcium signaling and transport is important for OL differentiation.

Calcium homeostasis can be another layer of regulation for OPC cell cycle. Silencing Cav1.2 calcium channels mediating voltage-gated Ca^{2+} influx was shown to extend cell cycle phases in OPCs to block differentiation (Cheli et al., 2015). In line with the observation, we showed that activating Ca^{2+} transportation with the calcium channel agonist Bay K 8644 reduced the number of proliferating OPCs. Taken together, the reduced expression of cell cycle regulators and Ca^{2+} ion channels contribute to OPC proliferation defects in developing *Tet1* cKO animals.

TET1-deficient OL lineage cells alter neuronal properties in a non–cell autonomous manner

Our results revealed a downregulation of a set of genes encoding neuronal regulatory factors, including GDNF, Reelin and Tenascin R, in *Tet1* cKO OPCs. GDNF can regulate neuronal synaptogenesis, especially the clustering of vesicular proteins and neurotransmitter transporters in presynaptic differentiation (Ledda et al., 2007). GDNF infusion has been shown to improve Parkinson's diseases potentially via strengthening of presynaptic synapses or numbers (Kirkeby and Barker, 2019; Patel et al., 2013). Consistent with its role in glia-neuron crosstalk, an electrophysiology study revealed that *Tet1* cKO brain exhibited an impaired postsynaptic transduction in excitatory neurons. The reduced frequency of EPSC in *Tet1* cKO combined with both the lack of any effect on synapse densities and the reduced expression of presynaptic components suggests that the ablation of *Tet1* in OL lineage cells may lead to defects in presynaptic release. These observations suggest that ablation of *Tet1* in OL lineage cells could lead to a defect in synaptic functions through a non-cell autonomous manner. This is in keeping with the observation that loss of methyl-CpG–binding protein 2 (MeCP2) in glial cells including oligodendrocytes impair neuronal properties and cause neuropathology in Rett syndrome (Ballas et al., 2009; Nguyen et al., 2013).

Altogether, our studies reveal critical epigenetic functions for TET1-5hmC in the regulation of stage-specific OL development and remyelination. We also identify a novel TET-mediated function

in OL homeostasis to maintain proper communication between OLs and neurons as well as neuronal properties and connectivity.

Acknowledgements

The authors would like to thank Dr. Fangfang Liu, Dr. Bo Zhao, Dr. Feng Zhang, Junjun Kang and Haifeng Zhang for technical support; Dr. Natalie Lai Man Wu for GSEA analysis; Dr. Weidong Tian, Dr. Feng Zhang, Dr. Yazhou Wang, Dr. Ceng Lou, Dr. Jinxiang Dai and Dr. Yaqi Deng for great comments; Dr. Guoliang Xu for *Tet1*^{loxp} lines. This work was funded by grants from National Natural Science Foundation of China (Grant number: 31571050 and 31371077) and Shaanxi Province Science and Technology Research and Development Projects (#2014KJXX-57) to X.Z, and US National Institutes of Health R01NS072427 and R01NS075243 to Q.R.L.

References:

Agresti, C., Meomartini, M.E., Amadio, S., Ambrosini, E., Serafini, B., Franchini, L., Volonte, C., Aloisi, F., and Visentin, S. (2005). Metabotropic P2 receptor activation regulates oligodendrocyte progenitor migration and development. Glia *50*, 132-144.

Ballas, N., Lioy, D.T., Grunseich, C., and Mandel, G. (2009). Non-cell autonomous influence of MeCP2-deficient glia on neuronal dendritic morphology. Nat Neurosci *12*, 311-317.

Baraban, M., Koudelka, S., and Lyons, D.A. (2018). Ca (2+) activity signatures of myelin sheath formation and growth in vivo. Nat Neurosci *21*, 19-23.

Bennin, D.A., Don, A.S., Brake, T., McKenzie, J.L., Rosenbaum, H., Ortiz, L., DePaoli-Roach, A.A., and Horne, M.C. (2002). Cyclin G2 associates with protein phosphatase 2A catalytic and regulatory B' subunits in active complexes and induces nuclear aberrations and a G1/S phase cell cycle arrest. The Journal of biological chemistry *277*, 27449-27467.

Bernstein, B.E., Mikkelsen, T.S., Xie, X., Kamal, M., Huebert, D.J., Cuff, J., Fry, B., Meissner, A., Wernig, M., Plath, K.*, et al.* (2006). A bivalent chromatin structure marks key developmental genes in embryonic stem cells. Cell *125*, 315-326.

Boutros, R., Mondesert, O., Lorenzo, C., Astuti, P., McArthur, G., Chircop, M., Ducommun, B., and Gabrielli, B. (2013). CDC25B overexpression stabilises centrin 2 and promotes the formation of excess centriolar foci. PLoS One *8*, e67822.

Butt, A.M. (2006). Neurotransmitter-mediated calcium signalling in oligodendrocyte physiology and pathology. Glia *54*, 666-675.

Chan, J.R., Watkins, T.A., Cosgaya, J.M., Zhang, C., Chen, L., Reichardt, L.F., Shooter, E.M., and Barres, B.A. (2004). NGF controls axonal receptivity to myelination by Schwann cells or oligodendrocytes. Neuron *43*, 183-191.

Cheli, V.T., Santiago Gonzalez, D.A., Namgyal Lama, T., Spreuer, V., Handley, V., Murphy, G.G., and Paez, P.M. (2016). Conditional Deletion of the L-Type Calcium Channel Cav1.2 in Oligodendrocyte Progenitor Cells Affects Postnatal Myelination in Mice. The Journal of neuroscience : the official journal of the Society for Neuroscience *36*, 10853-10869.

Cheli, V.T., Santiago Gonzalez, D.A., Spreuer, V., and Paez, P.M. (2015). Voltage-gated Ca2+ entry promotes oligodendrocyte progenitor cell maturation and myelination in vitro. Exp Neurol *265*, 69-83.

Chen, Y., Wu, H., Wang, S., Koito, H., Li, J., Ye, F., Hoang, J., Escobar, S.S., Gow, A., Arnett, H.A.*, et al.* (2009). The oligodendrocyte-specific G protein-coupled receptor GPR17 is a cell-intrinsic timer of myelination. Nat Neurosci *12*, 1398-1406.

Chrysanthou, S., Senner, C.E., Woods, L., Fineberg, E., Okkenhaug, H., Burge, S., Perez-Garcia, V., and Hemberger, M. (2018). A Critical Role of TET1/2 Proteins in Cell-Cycle Progression of Trophoblast Stem Cells. Stem cell reports.

Devaux, J., Gola, M., Jacquet, G., and Crest, M. (2002). Effects of K+ channel blockers on developing rat myelinated CNS axons: identification of four types of K+ channels. J Neurophysiol *87*, 1376-1385.

Devaux, J., and Gow, A. (2008). Tight junctions potentiate the insulative properties of small CNS myelinated axons. J Cell Biol *183*, 909-921.

Down, T.A., Rakyan, V.K., Turner, D.J., Flicek, P., Li, H., Kulesha, E., Graf, S., Johnson, N., Herrero, J., Tomazou, E.M.*, et al.* (2008). A Bayesian deconvolution strategy for immunoprecipitation-based DNA methylome analysis. Nat Biotechnol *26*, 779-785.

Emery, B., and Lu, Q.R. (2015). Transcriptional and Epigenetic Regulation of Oligodendrocyte Development and Myelination in the Central Nervous System. Cold Spring Harbor perspectives in biology *7*, a020461.

Evans, R.D., Weston, D.A., McLaughlin, M., and Brown, A.M. (2010). A non-linear regression analysis method for quantitative resolution of the stimulus-evoked compound action potential from rodent optic nerve. Journal of neuroscience methods *188*, 174-178.

Ferrer-Ferrer, M., and Dityatev, A. (2018). Shaping Synapses by the Neural Extracellular Matrix.

Frontiers in neuroanatomy *12*, 40.
Ficz, G., Branco, M.R., Seisenberger, S., Santos, F., Krueger, F., Hore, T.A., Marques, C.J., Andrews, S., and Reik, W. (2011). Dynamic regulation of 5-hydroxymethylcytosine in mouse ES cells and during differentiation. Nature *473*, 398-U589.
Friess, M., Hammann, J., Unichenko, P., Luhmann, H.J., White, R., and Kirischuk, S. (2016). Intracellular ion signaling influences myelin basic protein synthesis in oligodendrocyte precursor cells. Cell Calcium *60*, 322-330.
Gopalakrishnan, S., Van Emburgh, B.O., and Robertson, K.D. (2008). DNA methylation in development and human disease. Mutation research *647*, 30-38.
Graff, J., Kim, D., Dobbin, M.M., and Tsai, L.H. (2011). Epigenetic regulation of gene expression in physiological and pathological brain processes. Physiol Rev *91*, 603-649.
Greenberg, D.A., Cooper, E.C., and Carpenter, C.L. (1984). Calcium channel 'agonist' BAY K 8644 inhibits calcium antagonist binding to brain and PC12 cell membranes. Brain Res *305*, 365-368.
Gregath, A., and Lu, Q.R. (2018). Epigenetic modifications-insight into oligodendrocyte lineage progression, regeneration, and disease. FEBS letters *592*, 1063-1078.
Gu, T.P., Guo, F., Yang, H., Wu, H.P., Xu, G.F., Liu, W., Xie, Z.G., Shi, L., He, X., Jin, S.G*., et al.* (2011). The role of Tet3 DNA dioxygenase in epigenetic reprogramming by oocytes. Nature *477*, 606-610.
Hahn, M.A., Qiu, R., Wu, X., Li, A.X., Zhang, H., Wang, J., Jui, J., Jin, S.G., Jiang, Y., Pfeifer, G.P*., et al.* (2013). Dynamics of 5-hydroxymethylcytosine and chromatin marks in Mammalian neurogenesis. Cell Rep *3*, 291-300.
Hornig, J., Frob, F., Vogl, M.R., Hermans-Borgmeyer, I., Tamm, E.R., and Wegner, M. (2013). The transcription factors Sox10 and Myrf define an essential regulatory network module in differentiating oligodendrocytes. PLoS genetics *9*, e1003907.
Huang, S., Zhu, Z., Wang, Y., Wang, Y., Xu, L., Chen, X., Xu, Q., Zhang, Q., Zhao, X., Yu, Y*., et al.* (2013). Tet1 is required for Rb phosphorylation during G1/S phase transition. Biochemical and biophysical research communications *434*, 241-244.
Ito, S., D'Alessio, A.C., Taranova, O.V., Hong, K., Sowers, L.C., and Zhang, Y. (2010). Role of Tet proteins in 5mC to 5hmC conversion, ES-cell self-renewal and inner cell mass specification. Nature *466*, 1129-1133.
Iurlaro, M., von Meyenn, F., and Reik, W. (2017). DNA methylation homeostasis in human and mouse development. Current opinion in genetics & development *43*, 101-109.
Kalaszczynska, I., Geng, Y., Iino, T., Mizuno, S., Choi, Y., Kondratiuk, I., Silver, D.P., Wolgemuth, D.J., Akashi, K., and Sicinski, P. (2009). Cyclin A is redundant in fibroblasts but essential in hematopoietic and embryonic stem cells. Cell *138*, 352-365.
Khoueiry, R., Sohni, A., Thienpont, B., Luo, X., Velde, J.V., Bartoccetti, M., Boeckx, B., Zwijsen, A., Rao, A., Lambrechts, D*., et al.* (2017). Lineage-specific functions of TET1 in the postimplantation mouse embryo. Nature genetics *49*, 1061-1072.
Kirischuk, S., Scherer, J., Kettenmann, H., and Verkhratsky, A. (1995). Activation of P2-purinoreceptors triggered Ca2+ release from InsP3-sensitive internal stores in mammalian oligodendrocytes. J Physiol *483 (Pt 1)*, 41-57.
Kirkeby, A., and Barker, R.A. (2019). Parkinson disease and growth factors - is GDNF good enough? Nature reviews Neurology *15*, 312-314.
Krasnow, A.M., Ford, M.C., Valdivia, L.E., Wilson, S.W., and Attwell, D. (2018). Regulation of developing myelin sheath elongation by oligodendrocyte calcium transients in vivo. Nat Neurosci *21*, 24-28.
Kriaucionis, S., and Heintz, N. (2009). The nuclear DNA base 5-hydroxymethylcytosine is present in Purkinje neurons and the brain. Science *324*, 929-930.
Larson, V.A., Zhang, Y., and Bergles, D.E. (2016). Electrophysiological properties of NG2(+) cells: Matching physiological studies with gene expression profiles. Brain Res *1638*, 138-160.
Ledda, F., Paratcha, G., Sandoval-Guzman, T., and Ibanez, C.F. (2007). GDNF and GFRalpha1 promote formation of neuronal synapses by ligand-induced cell adhesion. Nat Neurosci *10*, 293-300.

Li, T., Wang, L., Ma, T., Wang, S., Niu, J., Li, H., and Xiao, L. (2018). Dynamic Calcium Release From Endoplasmic Reticulum Mediated by Ryanodine Receptor 3 Is Crucial for Oligodendroglial Differentiation. Frontiers in molecular neuroscience *11*, 162.
Li, X., Yao, B., Chen, L., Kang, Y., Li, Y., Cheng, Y., Li, L., Lin, L., Wang, Z., Wang, M.*, et al.* (2017). Ten-eleven translocation 2 interacts with forkhead box O3 and regulates adult neurogenesis. Nature communications *8*, 15903.
Liu, J., Moyon, S., Hernandez, M., and Casaccia, P. (2016). Epigenetic control of oligodendrocyte development: adding new players to old keepers. Current opinion in neurobiology *39*, 133-138.
Lu, G., Zhang, M., Wang, J., Zhang, K., Wu, S., and Zhao, X. (2019). Epigenetic regulation of myelination in health and disease. The European journal of neuroscience *49*, 1371-1387.
Lu, H., Liu, X., Deng, Y., and Qing, H. (2013). DNA methylation, a hand behind neurodegenerative diseases. Front Aging Neurosci *5*, 85.
Mogha, A., D'Rozario, M., and Monk, K.R. (2016). G Protein-Coupled Receptors in Myelinating Glia. Trends Pharmacol Sci *37*, 977-987.
Morita, J., Kano, K., Kato, K., Takita, H., Sakagami, H., Yamamoto, Y., Mihara, E., Ueda, H., Sato, T., Tokuyama, H.*, et al.* (2016). Structure and biological function of ENPP6, a choline-specific glycerophosphodiester-phosphodiesterase. Scientific reports *6*, 20995.
Moyon, S., Huynh, J.L., Dutta, D., Zhang, F., Ma, D., Yoo, S., Lawrence, R., Wegner, M., John, G.R., Emery, B.*, et al.* (2016). Functional Characterization of DNA Methylation in the Oligodendrocyte Lineage. Cell Rep.
Moyon, S., Ma, D., Huynh, J.L., Coutts, D.J.C., Zhao, C., Casaccia, P., and Franklin, R.J.M. (2017). Efficient Remyelination Requires DNA Methylation. eNeuro *4*.
Nagi Ayad, S.R., Monica Murakami, Judith Jebanathirajah,Steven Gygi,and Marc W. Kirschner (2003). Tome-1, a Trigger of Mitotic Entry, Is Degraded during G1 via the APC. Cell.
Nave, K.A., and Werner, H.B. (2014). Myelination of the nervous system: mechanisms and functions. Annu Rev Cell Dev Biol *30*, 503-533.
Neri, F., Incarnato, D., Krepelova, A., Rapelli, S., Pagnani, A., Zecchina, R., Parlato, C., and Oliviero, S. (2013). Genome-wide analysis identifies a functional association of Tet1 and Polycomb repressive complex 2 in mouse embryonic stem cells. Genome Biol *14*, R91.
Nguyen, M.V., Felice, C.A., Du, F., Covey, M.V., Robinson, J.K., Mandel, G., and Ballas, N. (2013). Oligodendrocyte lineage cells contribute unique features to Rett syndrome neuropathology. J Neurosci *33*, 18764-18774.
Pastor, W.A., Pape, U.J., Huang, Y., Henderson, H.R., Lister, R., Ko, M., McLoughlin, E.M., Brudno, Y., Mahapatra, S., Kapranov, P.*, et al.* (2011). Genome-wide mapping of 5-hydroxymethylcytosine in embryonic stem cells. Nature *473*, 394-397.
Patel, N.K., Pavese, N., Javed, S., Hotton, G.R., Brooks, D.J., and Gill, S.S. (2013). Benefits of putaminal GDNF infusion in Parkinson disease are maintained after GDNF cessation. Neurology *81*, 1176-1178.
Pinheiro, P.S., and Mulle, C. (2008). Presynaptic glutamate receptors: physiological functions and mechanisms of action. Nature reviews Neuroscience *9*, 423-436.
Shi, D.Q., Ali, I., Tang, J., and Yang, W.C. (2017). New Insights into 5hmC DNA Modification: Generation, Distribution and Function. Frontiers in genetics *8*, 100.
Smith, Z.D., and Meissner, A. (2013). DNA methylation: roles in mammalian development. Nat Rev Genet *14*, 204-220.
Stevens, B., Porta, S., Haak, L.L., Gallo, V., and Fields, R.D. (2002). Adenosine: a neuron-glial transmitter promoting myelination in the CNS in response to action potentials. Neuron *36*, 855-868.
Stroud, H., Feng, S.H., Kinney, S.M., Pradhan, S., and Jacobsen, S.E. (2011). 5-Hydroxymethylcytosine is associated with enhancers and gene bodies in human embryonic stem cells. Genome Biol *12*.
Stys, P.K., Ransom, B.R., and Waxman, S.G. (1991). Compound action potential of nerve recorded by suction electrode: a theoretical and experimental analysis. Brain Res *546*, 18-32.
Sun, W., Zang, L., Shu, Q., and Li, X. (2014). From development to diseases: the role of 5hmC in

brain. Genomics *104*, 347-351.
Szulwach, K.E., Li, X., Li, Y., Song, C.X., Han, J.W., Kim, S., Namburi, S., Hermetz, K., Kim, J.J., Rudd, M.K.*, et al.* (2011a). Integrating 5-hydroxymethylcytosine into the epigenomic landscape of human embryonic stem cells. PLoS genetics *7*, e1002154.
Szulwach, K.E., Li, X., Li, Y., Song, C.X., Wu, H., Dai, Q., Irier, H., Upadhyay, A.K., Gearing, M., Levey, A.I.*, et al.* (2011b). 5-hmC-mediated epigenetic dynamics during postnatal neurodevelopment and aging. Nat Neurosci *14*, 1607-1616.
Tahiliani, M., Koh, K.P., Shen, Y., Pastor, W.A., Bandukwala, H., Brudno, Y., Agarwal, S., Iyer, L.M., Liu, D.R., Aravind, L.*, et al.* (2009). Conversion of 5-methylcytosine to 5-hydroxymethylcytosine in mammalian DNA by MLL partner TET1. Science *324*, 930-935.
Tan, L., Xiong, L., Xu, W., Wu, F., Huang, N., Xu, Y., Kong, L., Zheng, L., Schwartz, L., Shi, Y.*, et al.* (2013). Genome-wide comparison of DNA hydroxymethylation in mouse embryonic stem cells and neural progenitor cells by a new comparative hMeDIP-seq method. Nucleic Acids Res *41*, e84.
Timofeev, O., Cizmecioglu, O., Settele, F., Kempf, T., and Hoffmann, I. (2010). Cdc25 phosphatases are required for timely assembly of CDK1-cyclin B at the G2/M transition. The Journal of biological chemistry *285*, 16978-16990.
Ventruti, A., Kazdoba, T.M., Niu, S., and D'Arcangelo, G. (2011). Reelin deficiency causes specific defects in the molecular composition of the synapses in the adult brain. Neuroscience *189*, 32-42.
Wang, F., Yang, Y.J., Yang, N., Chen, X.J., Huang, N.X., Zhang, J., Wu, Y., Liu, Z., Gao, X., Li, T.*, et al.* (2018). Enhancing Oligodendrocyte Myelination Rescues Synaptic Loss and Improves Functional Recovery after Chronic Hypoxia. Neuron *99*, 689-701 e685.
Wang, W., Li, C., Chen, Q., van der Goes, M.S., Hawrot, J., Yao, A.Y., Gao, X., Lu, C., Zang, Y., Zhang, Q.*, et al.* (2017). Striatopallidal dysfunction underlies repetitive behavior in Shank3-deficient model of autism. The Journal of clinical investigation *127*, 1978-1990.
Wasser, C.R., and Herz, J. (2017). Reelin: Neurodevelopmental Architect and Homeostatic Regulator of Excitatory Synapses. The Journal of biological chemistry *292*, 1330-1338.
Williams, K., Christensen, J., Pedersen, M.T., Johansen, J.V., Cloos, P.A., Rappsilber, J., and Helin, K. (2011). TET1 and hydroxymethylcytosine in transcription and DNA methylation fidelity. Nature *473*, 343-348.
Wu, H., D'Alessio, A.C., Ito, S., Xia, K., Wang, Z., Cui, K., Zhao, K., Sun, Y.E., and Zhang, Y. (2011). Dual functions of Tet1 in transcriptional regulation in mouse embryonic stem cells. Nature *473*, 389-393.
Xin, M., Yue, T., Ma, Z., Wu, F.F., Gow, A., and Lu, Q.R. (2005). Myelinogenesis and axonal recognition by oligodendrocytes in brain are uncoupled in Olig1-null mice. The Journal of neuroscience : the official journal of the Society for Neuroscience *25*, 1354-1365.
Xu, Y.F., Wu, F.Z., Tan, L., Kong, L.C., Xiong, L.J., Deng, J., Barbera, A.J., Zheng, L.J., Zhang, H.K., Huang, S.*, et al.* (2011). Genome-wide Regulation of 5hmC, 5mC, and Gene Expression by Tet1 Hydroxylase in Mouse Embryonic Stem Cells. Mol Cell *42*, 451-464.
Yildirim, O., Li, R., Hung, J.H., Chen, P.B., Dong, X., Ee, L.S., Weng, Z., Rando, O.J., and Fazzio, T.G. (2011). Mbd3/NURD complex regulates expression of 5-hydroxymethylcytosine marked genes in embryonic stem cells. Cell *147*, 1498-1510.
Yu, Y., Chen, Y., Kim, B., Wang, H., Zhao, C., He, X., Liu, L., Liu, W., Wu, L.M., Mao, M.*, et al.* (2013). Olig2 targets chromatin remodelers to enhancers to initiate oligodendrocyte differentiation. Cell *152*, 248-261.
Zeisel, A., Munoz-Manchado, A.B., Codeluppi, S., Lonnerberg, P., La Manno, G., Jureus, A., Marques, S., Munguba, H., He, L., Betsholtz, C.*, et al.* (2015). Brain structure. Cell types in the mouse cortex and hippocampus revealed by single-cell RNA-seq. Science *347*, 1138-1142.
Zhang, M., Liu, Y., Wu, S., and Zhao, X. (2019). Ca(2+) Signaling in Oligodendrocyte Development. Cellular and molecular neurobiology *39*, 1071-1080.
Zhang, R.R., Cui, Q.Y., Murai, K., Lim, Y.C., Smith, Z.D., Jin, S., Ye, P., Rosa, L., Lee, Y.K., Wu, H.P.*, et al.* (2013). Tet1 regulates adult hippocampal neurogenesis and cognition. Cell Stem Cell *13*, 237-245.

Zhang, Y., Chen, K., Sloan, S.A., Bennett, M.L., Scholze, A.R., O'Keeffe, S., Phatnani, H.P., Guarnieri, P., Caneda, C., Ruderisch, N.*, et al.* (2014). An RNA-sequencing transcriptome and splicing database of glia, neurons, and vascular cells of the cerebral cortex. The Journal of neuroscience : the official journal of the Society for Neuroscience *34*, 11929-11947.

Zhao, X., Dai, J., Ma, Y., Mi, Y., Cui, D., Ju, G., Macklin, W.B., and Jin, W. (2014). Dynamics of ten-eleven translocation hydroxylase family proteins and 5-hydroxymethylcytosine in oligodendrocyte differentiation. Glia *62*, 914-926.

Zhao, X., He, X., Han, X., Yu, Y., Ye, F., Chen, Y., Hoang, T., Xu, X., Mi, Q.S., Xin, M.*, et al.* (2010). MicroRNA-mediated control of oligodendrocyte differentiation. Neuron *65*, 612-626.

Zhu, X., Hill, R.A., Dietrich, D., Komitova, M., Suzuki, R., and Nishiyama, A. (2011). Age-dependent fate and lineage restriction of single NG2 cells. Development *138*, 745-753.

Zuchero, J.B., and Barres, B.A. (2013). Intrinsic and extrinsic control of oligodendrocyte development. Current opinion in neurobiology *23*, 914-920.

Methods

Animals, Immunohistochemistry and electron microscopy

All animal experiment protocols were approved by the Animal Care and Use Committee of the Fourth Medical University and were conducted in accordance with the guidelines for the care and use of laboratory animals. *Tet1* $^{flox/flox}$ mice (Zhang et al., 2013) and *Tet3* $^{flox/flox}$ mice (Gu et al., 2011) were crossed with heterozygous *Olig1*-Cre mice (Xin et al., 2005; Yu et al., 2013) to generate *Tet1*$^{flox/+}$;*Olig1*Cre$^{+/-}$ mice and *Tet3*$^{flox/+}$;*Olig1*Cre$^{+/-}$ mice, which were then bred with *Tet1*$^{flox/flox}$ mice or *Tet3*$^{flox/flox}$ to produce *Tet1* cKO (*Tet1*$^{flox/flox}$;*Olig1*Cre$^{+/-}$) or *Tet3* cKO (*Tet3*$^{flox/flox}$;*Olig1*Cre$^{+/-}$) offspring, respectively. *NG2CreER*^{T} mice (Zhu et al., 2011) were from Jackson lab.

For immunohistochemistry, cryosections (14μm) of brains or spinal cords were short-fixed 30 min in 4% paraformaldehyde and processed for antigen retrieval. Sections were treated with 10mM sodium citrate (pH6.0) at ~90°C for 10min in a microwave and cooled down in room temperature. Then sections were washed three times in PBS, blocked in 3% BSA with 0.03% Triton X-100 (blocking buffer) for 1 hour (hr) at RT, and incubated with primary antibodies in blocking buffer overnight at RT. Next day, sections were washed three times in PBS, incubated with secondary antibodies at RT for 2 hr, and then counter stained with DAPI for 5min. Finally, sections were washed three times in PBS and mounted. Images were taken on Olympus FV1200 Confocal microscope. We used antibodies against Olig2 (Millipore, AB9610), Sox10 (Santa Cruz, 17342), TET1 (Zhao et al., 2014), PDGFRα (Abcam, ab61219), CC1 (Oncogene Research, OP80), MBP (Abcam, ab7349), 5hmC (Active motif, 39769), ALDHL1 (Proteintech, 17390-1-AP), CNPase (Sigma, C5922), Ki67 (Abcam, ab16667), GFAP (Millipore, mAB360), GFP (Abcam, ab5450), GST-pi (Abcam, ab53943), DCX (Millipore, ab2253), MAP2 (Millipore,MAB364), Synaptophysin (CST, 5461), vGlut1 (Synaptic Systems,135303), Homer1 (Abcam, ab211415).

For BrdU pulse labeling, animals were injected intraperitoneally with 100 mg BrdU/kg body weight 2 hr prior to sacrifice. For the staining of BrdU, as well as 5hmC, before permeabilization, sections were subjected to DNA denaturation with 2N hydrochloric acid at 37 °C for 20 min and then neutralized with 0.1 M sodium borate at pH 8.5 for 2X 10 min. The G3G4 monoclonal antibody (anti BrdUrd) was obtained from the Developmental Studies Hybridoma Bank developed under the auspices of the NICHD and maintained by The University of Iowa.

For TUNEL/Olig2 double staining, Olig2 immunostaining were applied after DeadEnd™ Fluorometric TUNEL System kit (Promega, G2350) to reveal TUNEL positive cells in OL lineage.

Histological myelin staining was performed with Black Gold II Kit (Millipore, AG105) according to the user manual.

For electron microscopy, tissues were dissected and fixed in 2% glutaraldehyde and 4% paraformaldehyde in 0.1 M cacodylate buffer (pH 7.2) for 24 hr and processed as previously described (Zhao et al., 2010). Ultrathin sections were examined under the JEM-1230 electron microscope (JEOL LTD, Tokyo, Japan) equipped with CCD camera and its application software (832 SC1000, Gatan, Warrendale, PA).

Western blot assay

Immunoblotting were performed as described previously by our lab (Zhao et al., 2014). We used antibodies against Olig2 (Millipore MABN50), MBP (Abcam, ab7349), NeuN (Abcam, ab7349), ALDHL1 (Proteintech, 17390-1-AP), DCX (Proteintech, 13925-1-AP), Synaptophysin (CST, 5461), vGlut1 (CST, 12331), Homer1 (Abcam, ab211415), PSD95 (CST, 2507), GDNF (Boster Biological Technology, BM5124). β-actin (GuanXingYu, P1001) and Tubulin (Abbkine, A01030). The band intensity was calculated with Tanon5200 imager, normalized to β-actin or Tubulin level expressed as relative fold change against control.

RNA Extraction and qRT-PCR

Total RNAs were purified from tissues or cell cultures using TRIzol reagent according to the manufacturer's instruction (Invitrogen). For qRT-PCR, RNA was transcribed to cDNA with the

PrimeScript™ RT reagent Kit (Perfect Real Time, Takara) and reactions were performed with SYBR® Premix Ex Taq™ (Takara) in CFX96 Touch Real-Time PCR Detection System (Bio-Rad). Relative gene expression was normalized to internal control β-actin. Primer sequences for SybrGreen probes of target genes are listed below.

Gene	Forward	Reverse
Ccna2	TGGATGGCAGTTTTGAATCACC	CCCTAAGGTACGTGTGAATGTC
Ccnb2	GCCAAGAGCCATGTGACTATC	CAGAGCTGGTACTTTGGTGTTC
Ccnf	AGAGACTGAATACGGGTTCTGA	TCCCAAGCAGTGTAGTATGGAA
Ccng2	AGGGGTTCAGCTTTTCGGATT	AGTGTTATCATTCTCCGGGGTAG
Cdc25b	TCCGATCCTTACCAGTGAGG	GGGCAGAGCTGGAATGAGG
Cdc25c	GGCAAACCTAAGCATTCTGTCG	CCAGAGGTCCAGATGAATCCA
Cdca3	CTGAGCGAAGTATTGGAGACAG	CTGCGGATTGTTTGGCTTCC
Cdk19	GGTCAAGCCTGACAGCAAAGT	TTCCTGGAAGTAAGGGTCCTG
Cldn11	ATGGTAGCCACTTGCCTTCAG	AGTTCGTCCATTTTTCGGCAG
Enpp2	TTTGCACTATGCCAACAATCGG	GGAGGCACTTTAGTCCTGTACTT
Kif11	GGCTGGTATAATTCCACGCAC	CCGGGGATCATCAAACATCTG
Mbp	GCAGCCAGCACCACTCTTGA	CAGCCGAGGTCCCATTGTTC
Myrf	CCTGTGTCCGTGGTACTGTG	TCACACAGGCGGTAGAAGTG
Cnp	TTTACCCGCAAAAGCCACACA	CACCGTGTCCTCATCTTGAAG
Ugt8a	ACTCCATATTTCATGCTCCTGTG	AGGCCGATGCTAGTGTCTTGA
Plp1	CCAGAATGTATGGTGTTCTCCC	GGCCCATGAGTTTAAGGACG
Bcas1	AGAAGCGAAAGGCTCGGAAG	AGGGACAGAATAACTCAGAGTGT
Tet1	CATTCTCACAAGGACATTCACAACA	AGTAAAACGTAGTCGCCTCTTCCTG
β-actin	GGCTGTATTCCCCTCCATCG	CCAGTTGGTAACAATGCCATGT
Ccl22	AGGTCCCTATGGTGCCAATGT	CGGCAGGATTTTGAGGTCCA
Ccl2	TCAAACTGAAGCTCGCACTCT	GGGGCATTGATTGCATCTGG
Ccr2	ATCCACGGCATACTATCAACATC	CAAGGCTCACCATCATCGTAG
Cx3cr1	GAGTATGACGATTCTGCTGAGG	CAGACCGAACGTGAAGACGAG
Itpr2	CCTCGCCTACCACATCACC	TCACCACTCTCACTATGTCGT
Cacna1a	CACCGAGTTTGGGAATAACTTCA	ATTGTGCTCCGTGATTTGGAA
Cacna1c	ATTGTGCTCCGTGATTTGGAA	ACTGACGGTAGAGATGGTTGC
Cacna2d1	GTCACACTGGATTTTCTCGATGC	GGGTTTCTGAATATCTGGCCTGA

Cacnb4	TACCTGCATGGAGTTGAAGACT	TTCGCTCTCTCAAGCTGGATA
Cacng5	ACCTGGAAGAAGGCATAATCCT	CTATGGTAAAACAGCGTCCTCG
Atp2b1	AGATGGAGCTATTGAGAATCGCA	CCCTGTAACACGGATTTTTCCTT
Atp2c1	GCAGGCAGAAGAAGCACCAA	CCTAGTAACCAGCCAACCAAC
Slc8a1	CTTCCCTGTTTGTGCTCCTGT	AGAAGCCCTTTATGTGGCAGTA
Gdnf	TCCAACTGGGGGTCTACGG	GCCACGACATCCCATAACTTCAT
Reln	TTACTCGCACCTTGCTGAAAT	CAGTTGCTGGTAGGAGTCAAAG
Tnr	GGCTGGAGGTGACTACAGAAA	GAAGACCATAGGCTGTTCCTTG
Ank3	ACCAAATACGTGTGGAAAATCCC	GTTCTGCCAACCATCAACTGG

Culture of OL precursor cells, immunocytochemistry and ELISA assay

Mouse OPCs were isolated from P6 cortices of mice by immunopanning with antibodies against Ran-2, GalC and O4 sequentially as previously described (Chan et al., 2004). Briefly, cerebral hemispheres were diced and digested with papain at 37°C. Following gentle trituration, cells were resuspended in a panning buffer containing insulin (5 µg/ml) and then incubated at room temperature sequentially on three immunopanning dishes: Ran-2, anti-GalC, and O4. $O4^{+}GalC^{-}$ OPCs were released from the final panning dish with trypsin (Sigma).

For immunocytochemistry, cell cultures were fixed in 4% PFA. After TritonX-100 permeabilization for 15 min, samples were incubated with primary antibody for 1 h at room temperature followed by fluorescent secondary antibody for another hour. Cells were then counter-stained with DAPI and visualized with Confocal microscope. Experiments were replicated using cells from three different primary cultures.

GDNF ELISA (enzyme-linked immunosorbent assay) was performed using commercial kits (EK 0935, Boster Biological Technology, Wuhan, China) following the manufacturer's instructions. Culture supernatant from $10^5/cm^2$ OPCs were collected after 24hr incubation and sterilized by filtering through 0.22 µm filters. Synthetic mouse GDNF peptide was used to generate a standard curve for each experiment. The plates were developed using the TMB substrate, and the reaction was stopped by addition of equal volume of STOP buffer. The results were read using Infinite M200 Pro colorimetric plate reader (TECAN, Austria).

Flow cytometric analysis of cell cycle with propidium iodide DNA staining

PI staining for flow cytometry was performed according to the user manual of DNA Content Quantitation Assay (Cell Cycle) from Solarbio (#CA1510). Briefly, OPCs from control or *Tet1* cKO mice were harvested, washed in PBS and fixed in cold 70% ethanol for 30 min at 4°C. After wash twice in PBS, cells were treated with RNase and then stained with PI. With guava easyCyte6HT (Millipore), the forward scatter (FS) and side scatter (SS) were measured to identify single cells. For analysis, ModFit LT software was used make the PI histogram plot. Experiments were replicated three times.

Lysolecithin-induced demyelinating injury

Lysolecithin-induced demyelination was carried out in the corpus callosum of 8-week-old mice. Anesthesia was induced and maintained by peritoneal injection of a mixture of ketamine (90 mg/kg) and xylazine (10 mg/kg). The skull was exposed, and a hole was cut into the cranium. Focal demyelinating lesions were induced by stereotaxic injection of 0.8 µl 1%lysolecithin solution (L-a-lysophosphatidylcholine, Sigma L4129) into the corpus callosum at coordinates: 0.8 mm lateral, 0.8 mm rostral to bregma, 1.2mm deep to brain surface) using a glass-capillary connected to a 10 µl

Hamilton syringe. Animals were left to recover in a warm chamber before being returned into their housing cages. LPC-induced injuries were conducted in a genotype-blinded manner.

Electrophysiology

Analyzing the compound action potential was performed according to previous protocols (Devaux and Gow, 2008; Evans et al., 2010). *Tet1* cKO and control littermates were killed by cervical dislocation and then decapitated. Optic nerves were dissected free and cut between the orbit and the optic chiasm in the standard artificial cerebrospinal fluid (aCSF) containing (in mM): NaCl 126, KCl 3.0, $CaCl_2$ 2.0, $MgCl_2$ 2.0, NaH_2PO4 1.2, $NaHCO_3$ 26 and glucose 10 at 37℃. Following dissection, optic nerves were equilibrated in aCSF for at least 30 min with constant aeration (95% O_2/5% CO_2). Then the nerve was gently placed in a customized perfusion chamber, maintained at 37℃ and perfused with aCSF at 2-3ml/min speed. Suction electrodes back-filled with aCSF were used for stimulation and recording. One electrode was attached to the rostral end of the nerve for stimulation and the second suction electrode was attached to the caudal end of the nerve to record the CAP, thus all recordings were orthodromic. Stimulus pulse strength (100μs duration, SS-201J Isolator constant current output with SEN-7203 stimulator, Nihon Kohden, Japan) was adjusted to evoke the maximum CAP possible and then increased another 25% (i.e. supramaximal stimulation). During an experiment, the supra maximal CAP was elicited every 10s and repeat 10 times. The signal was amplified 100×AC membrane potential (100mV/mV) by a Multiclamp700B amplifier, filtered at 10 kHz and acquired at 10 kHz (Digidata 1322A, Molecular Devices, USA). The average CAP amplitude and area were measured in Clampfit 10.0 software (Molecular Devices, USA) offline and performed blind to genotype. Image drawing and statistical analysis were performed in GraphPad Prism 6.

Whole-cell patch clamp recordings were conducted as previously described (Wang et al., 2017). Briefly, coronal slices (~300μm) were prepared from P21 mice with VT1200s vibrotome (Leica, Germany) and incubated at 32℃ with carbogenated aCSF for 10 to 15 minutes. For all the synaptic activity measurements, the slices were constantly perfused with carbogenated aCSF at room temperature. Whole-cell patch clamp recordings were performed in the layer 2/3 neurons of the M2 region verified with BX51WI microscope (Olympus, Japan) with infrared differential interference contrast (IR-DIC) visual guide. Neurons were held at a membrane potential of −70 mV with a Muticlamp 700B amplifier and characterized by injection of rectangular voltage pulse (5 mV, 50 ms) to monitor the whole-cell membrane capacitance, series resistance and membrane resistance. Pipettes were filled with the internal solution containing the following: 110 CsOH (50% wt), d-gluconic acid (49%–53% wt), 4 mM NaCl, 15 mM KCl, 5 mM TEA-Cl, 20 mM HEPES, 0.2 mM EGTA, 5 mM lidocaine N-ethyl chloride, 4 mM ATP magnesium salt, and 0.3 mM GTP sodium salt. pH was adjusted to 7.2-7.4 with CsOH, and osmolarity was adjusted to 298-300 mOsm with K_2SO_4 (approximately 8-10 mM). Cells were excluded from the study if the series resistance (Rs) changed by more than 20%. In addition, cells with Rs of more than 20 MΩ at any time during the recordings were discarded. sEPSC or mEPSCs were recorded 5 minutes after entering whole-cell patch-clamp recording mode, without or with pre-addition of 1 μM tetrodotoxin (TTX) and 100 μM picrotoxin to the aCSF. Signals were low-pass filtered at 2 kHz and sampled at 10 kHz with a Digidata 1322A. Data analysis was conducted in Clampfit 10.0 software and performed blind to genotype.

RNA-Seq and Data Analysis

RNA-seq assays were performed by RiboBio Co., Ltd. (Guangzhou, China). Briefly, libraries were prepared using Illumina RNA-Seq Preparation Kit (TruSeq RNA Sample Prep Kit) and sequenced by HiSeq 3000 sequencer. RNA-seq reads were mapped using TopHat with settings of “read mismatches=2” and “read gap length=2” (http://ccb.jhu.edu/software/tophat/ index.shtml). TopHat output data were then analyzed by DEGseq to compare the changes of gene expression between *Tet1 cKO* and control, based on the calculate RPKM values for known transcripts in mouse genome reference. Heatmap of gene differential expression was generated using R Package (http://www.r-

project.org).

hMeDIP-Sequencing analysis

hMeDIP Sequencing service was provided by KangChen Bio-tech (Shanghai, China). hMeDIP-Sequencing library preparation was performed according to a previous study(Down et al., 2008) with minor modifications. Genomic DNA was sonicated to ~200-800bp with a Bioruptor sonicator (Diagenode). 800 ng of sonicated DNA was end-repaired, A-tailed, and ligated to single-end adapters following the standard Illumina genomic DNA protocol (FC-102-1002, Illumina). After agarose size-selection to remove unligated adapters, the adaptor-ligated DNA was used for immunoprecipitation (IP) with a mouse monoclonal anti-5-hydroxymethylcytosine antibody (Diagenode, C15200200). For this, DNA was heat-denatured at 94°C for 10 min, rapidly cooled on ice, and immunoprecipitated with 1 µL primary antibody overnight at 4°C with rocking agitation in 400 µL IP buffer (0.5% BSA in PBS). To recover the immunoprecipitated DNA fragments, 20 µL of magnetic beads were added and incubated for an additional 2 hours at 4°C with agitation. After IP, a total of five washes were performed with ice-cold IP buffer. Washed beads were resuspended in TE buffer with 0.25% SDS and 0.25 mg/mL proteinase K for 2 hours at 65°C and then allowed to cool down to room temperature. DNA was then purified using Qiagen MinElute columns and eluted in 16 µL EB (Qiagen). 14 cycles of PCR were performed on 5 µL of the immunoprecipitated DNA using the single-end Illumina PCR primers. The resulting products were purified with Qiagen MinElute columns, after which a final size selection (300-1,000 bp) was performed by electrophoresis in 2% agarose. Libraries were quality controlled by Agilent 2100 Bioanalyzer.

For sequencing, the library was denatured with 0.1 M NaOH to generate single-stranded DNA molecules and loaded onto channels of the flow cell at 8 pM concentration, amplified in situ using TruSeq Rapid SRCluster Kit (GD-402-4001, Illumina). Sequencing was carried out by running 150 cycles on Illumina HiSeq 2500 using TruSeq Rapid SBS Kit (FC-402-4001, Illumina) according to the manufacturer's instructions.

After sequencing images generated, the stages of image analysis and base calling were performed using Off-Line Base caller software (OLB V1.8). After passing Solexa CHASTITY quality filter, the clean reads were aligned to Mus_musculus genome (UCSC mm10) using BOWTIE software (V2.1.0). Aligned reads were used for peak calling, both mRNA and LncRNA associated hMeDIP enriched regions (peaks) with statistically significant were identified for each sample, using a q-value threshold of 10^{-4} by MACS v2. Both mRNA and LncRNA associated hMeDIP enriched regions (peaks) were annotated by the nearest gene using the newest UCSC RefSeq database. Differentially hydroxymethylated regions (DhMRs) between two groups with statistically significant were identified by diffReps (Cut-off: $\log_2$FC=1.0, p-value=10^{-4}). DhMRs were annotated by the nearest gene using the UCSC RefSeq and database of multiple databases integration.

$[Ca^{2+}]_i$ imaging

Fluo4 was used to measure $[Ca^{2+}]$i changes. To load cells with Ca^{2+} probe, cultures were incubated in standard artificial cerebrospinal fluid (aCSF) containing (in mM): NaCl 125, KCl 3.0, $CaCl_2$ 2.0, $MgCl_2$ 2.0, NaH_2PO4 1.25, $NaHCO_3$ 26 and glucose 20, supplemented with 0.03% Pluronic F-127 and 0.6µM cell-permeable form of indicator (Fluo4-AM, Invitrogen) for 20 min at 37℃. After loading, cells were transferred into recording chamber on the stage of Olympus FV1000 confocal inverted microscope equipped with phase contrast optics. Measurements started after at least 15 min storage in aCSF to ensure deesterification of indicators. Fluo4 was excited with 488 nm laser and emitted light was collected at 515 nm. A series of sections were collected every 500 ms, at 500 ms intervals, for 180 s in total. Pharmacological agents were directly added in aCSF: ATP (Sigma, 100µM) or Bay K 8644 (10 µM), 30s after the first image was taken. The images were analyzed using the Olympus FV10-ASW 4.1 software. Cell bodies were selected as regions of interest (ROI) and normalized changes of Fluo4 fluorescence intensities were calculated as $\Delta F/F=(F-F0)/F0$ (F, fluorescence intensity; $F0$, baseline intensity). Data were expressed as Mean ± standard error of the mean (SEM),

'N' represents the number of responding cells. Experiments were performed 3 times from different cultures and the results were pooled together for analysis. N>100 in ATP treatment group and N>70 in Bay K 8644 group. Significance was determined by unpaired *t* tests, using Prism 6.0 (Graphpad).

Statistical analysis

Numerical values were analyzed using Mean ± SEM and are presented as bar graphs. Group with equal variances and normal distribution were compared using Student's *t* test (unpaired) with SPSS 21.0. One-Way ANOVA with repeated-measures and Two-Way ANOVA were applied to the data when appropriate. Significance is denoted as $*p<0.05$, $**p<0.01$ or $***p<0.001$ in the figures.

Data availability

The transcriptome and DNA hydroxymethylation profiling dataset have been deposited in the Gene Expression Omnibus database (GSE122838).

Figure legends

Figure 1. 5hmC dynamics are highly associated with OL specific genes during development and ablation of *Tet1* in OL lineage cells results in defective OPC differentiation in the brain

(A) Venn diagram reveals the specifically hydroxymethylated genes in OPCs. Purified OPC cultures were subjected to hMeDIP-seq analysis and peaks in Promoter-TSS regions were compared to previously published hMeDIP-seq data for neural progenitor cells (NPC) cultures (Li et al., 2017). 1237 genes were found with specific 5hmC peaks in OPCs.

(B) GO analysis for genes with OPC specific 5hmC peaks in promoter-TSS region. Representative GO terms indicate their association with OL development.

(C) Snapshots comparing the 5hmC profiles for oligodendrocyte representative genes, *Cspg4* (chondroitin sulfate proteoglycan 4), *Mag* (myelin-associated glycoprotein) and *Elovl7* (elongation of very long chain fatty acids protein 7) in NPC and OPC.

(D) Snapshots comparing the 5hmC profiles for NPC representative genes, *Id2* (Inhibitor of DNA Binding 2), *Zfp28* (Zinc Finger Protein 28) and *Ngf* (Nerve growth factor) in NPC and OPC.

(E) Schematic diagram shows Cre-mediated excision of floxed *Tet1* exons encoding the critical catalytic domain for dioxygenase activity, modified from Zhang et al., 2013.

(F-G) Reduced expression of TET1 in Sox10$^+$ OLs from *Tet1* cKO mice. Representative immunostaining images revealed the significantly decreased expression of TET1 in Sox10 positive cells in P4 corpus collosum from *Tet1* cKO mice. Arrows indicate Sox10$^+$ cells in both groups (F). Scale bar, 20 μm. Quantification the percentage of TET1/Sox10 double positive cells among Sox10 positive oligodendrocytes in P4 corpus collosum. Data are mean±SEM (n=3 animals each group). ***, p<0.001 compared to control by Student's t test (G).

(H) Quantitative real time PCR identified the reduced expression of *Tet1* mRNA in OPCs purified from *Tet1* cKO mice brain. Data represent average transcript levels relative to control, after normalization±SEM for n=3 independent experiments each performed in triplicates. ***, p<0.001 compared to control by Student's t test.

(I-J) The number of mature oligodendrocytes was significantly decreased in *Tet1* cKO mice after birth and recovered in adult mice. Representative images of CC1 and Sox10 immunostaining in the corpus callosum of control and *Tet1* cKO groups at P8 and P27 (I). Quantification of CC1 positive cells (J) in P8, P21, P27 and 2M stages, respectively. Notably, in 2M old mice, the number of CC1$^+$ cells were comparable between groups. *, p<0.05 compared to control by Student's t test (n=3 animals for control and n=3 to 5 for mutant group). Scale bar in I, 50μm.

(K) Immunostaining of MBP in *Tet1* cKO and control mice at P16. Note the decreased staining intensity of MBP in cortex and corpus collosum of *Tet1* cKO mice. Scale bar, 100μm.

Figure 2. TET1 is required for OL myelination

(A-B) Depletion of *Tet1* attenuated the maturation of purified OPC cultures. Representative images of immunostaining with CNPase and MBP at 3 and 5 DIV after induction of differentiation (A). Quantification of CNPase$^+$ and MBP$^+$ cells among the cultures from control or *Tet1 cKO* mice (B). Data are mean± SEM (n=3 of independent experiments each group). *, p<0.05 compared to control by Student's t test. Scale bar, 50μm.

(C) Electron micrographs of optic nerves from control and *Tet1* cKO mice at P14. Scale bar, 2 μm.

(D) Quantification the number of myelinated axons in defined area from optic nerve in control and *Tet1* cKO mice. Data are mean ± SEM (n=3 animals each group). *, p<0.05 compared to control by Student's t test.

(E) Scatter plot of the G ratio from P14 optic nerves with axonal perimeter on the x-axis and G-ratio on the y-axis. Increased G-ratio was observed in *Tet1* cKO mice.

(F-L) Ultrastructure of myelin in corpus collosum from *Tet1* cKO mice. Representative images of electron micrographs of corpus collosum from control and *Tet1* cKO mice at P14, P27 and 2M (F). Scar bar, 0.5 μm. Quantification the number of myelinated axons in defined area from P14 (G), P27 (I) and 2M (K) control and *Tet1* cKO mice. Data are mean ± SEM (n=3 animals each group). ***,

p<0.001 compared to control by Student's *t* test. Scatter plot showing the G ratio in P14 (H), P27 (J) and 2M (L) mice, with axonal perimeter on the x-axis and G-ratio on the y-axis.

Figure 3. Defect of proliferation and cell cycle progression in OPCs from *Tet1* cKO mice

(A-B) Loss of TET1 results in less OL precursor cells from embryonic stage. Representative images of Sox10/ PDGFRα staining at P1 from both groups (A). Scale bar, 100μm. Quantification of PDGFRα positive cells in E15.5, P1, P6, P14 and 2M cortex (B). From P6, the number of OPCs was comparable between groups. Data are mean± SEM (n=3 animals each group) *, *p*<0.05 compared to control by Student's *t* test.

(C-D) The number of proliferating OPCs was increased in *Tet1* cKO mice. Representative images of BrdU and Olig2 double immunostaining in P1 control or *Tet1* cKO mice, which were pulse injected with BrdU 2 hrs before sacrifice (C). Scale bar, 100μm. Quantification of $BrdU^+$ cells within $Sox10^+$ OPC population revealed the increased number of $BrdU^+$ cells in *Tet1* mutant (D). Data are mean± SEM (n=3 animals each group). *, *p*<0.05 compared to control by Student's *t* test.

(E-G) OPCs from *Tet1* cKO mice were prone to stay in proliferating stage in culture. Representative images of double immunostaining OPC cultures with BrdU/Olig2, or Ki67/Sox10 to illustrate the proliferating cells in OL lineage (E). Scale bar, 50μm. Comparison the proportion of $Ki67^+$ (F) and $BrdU^+$ cells (G) among OPCs between control and *Tet1* cKO mice. Note the increased number of proliferating OPCs in *Tet1* cKO group. Data are mean± SEM (n=3 independent experiments each group). *, *p*<0.05 compared to control by Student's *t* test.

(H-I) Flow cytometry revealed abnormal cell cycle in OPCs from *Tet1* cKO mice. Representative diagram of flow cytometry with PI DNA staining in purified OPCs from control and *Tet1* mutant (H). Quantification the percentage of cells in each phase. The experiments were repeat three times for both groups. Data are mean± SEM (n=3 independent experiments each group). *, *p*<0.05 compared to control by Student's *t* test.

Figure 4. Impaired CNS remyelination in *Tet1* OPC-iKO mice

(A) Diagram showing the LPC injection site.

(B) TET1 and Olig2 immunostaining in non-lesion control and LPC lesion corpus callosum at dpl 7. Arrows indicate $TET1^+$/$Olig2^+$ cells. Scale bar, 50 μm.

(C) Quantification of $TET1^+$ cell density and the percentage of strong TET1 staining in $Olig2^+$ cells in LPC lesion sites at dpl 7. Data are presented as mean ±SEM. n = 4 controls and 4 mutant animals, * *p*<0.05, two-tailed unpaired Student's t test.

(D) Diagram showing TAM administration and LPC injection schedule in $NG2CreER^T$;$Tet1^{flox/flox}$ mice.

(E) Immunolabeling for PDGFRα and GST-pi in LPC lesions from control and *Tet1*-iKO mutants at dpl 7 and dpl 14, respectively. Dashed line indicates the border of lesion site. Scale bars, 50 μm.

(F) Quantification of $PDGFR\alpha^+$ OPCs in LPC lesion sites at dpl 7. Data are presented as mean ±SEM. n = 4 controls and 3 mutant animals, *p* = 0.848, two-tailed unpaired Student's t test.

(G) Quantification of GST-pi^+ OLs in LPC lesion sites at dpl 14 and 21. Data are presented as mean ±SEM. n = 4 controls and 4 mutant animals, ** *p*<0.01, two-tailed unpaired Student's t test.

(H) Immunostaining for MBP in contralateral side and LPC lesions side from control and *Tet1*-iKO corpus callosum at dpl 21. Scale bar, 100 μm.

(I-K) Ultrastructure of remyelinating axons from control and *Tet1*-iKO mutants at dpl 21. Representative images of electron micrographs in LPC injured lesions (I). Scar bar, 0.5 μm. Quantification the number of myelinated axons in defined area (J). Data are mean ± SEM (n=3 animals each group). ***, *p*<0.001 compared to control by Student's *t* test. Scatter plot showing the G ratio, with axonal perimeter on the x-axis and G-ratio on the y-axis (K).

Figure 5. Lack of *Tet1* alters the transcriptome profiles in OPCs

(A) Heatmap of representative RNA-Seq data from purified OPCs illustrating the differentially expressed genes between control and *Tet1* cKO, sequencing for each genotype was repeated once.

(B) GSEA analysis of OPC cultures from *Tet1* mutant and control mice for top differentially regulated

gene sets.
(C) GSEA plots show the representative upregulated gene sets in *Tet1* mutant, mitochondria gene module and chemokine signaling pathway.
(D) Quantitative real-time PCR validated the increased expression of chemokine genes in *Tet1* mutant. Data represent average transcript levels relative to control, after normalization as mean ± SEM for three independent experiments each performed in triplicates. *, $p<0.05$ compared to control by Student's *t* test.
(E) GSEA plots show the gene set of ensheathment of axons that is downregulated in *Tet1* mutant.
(F) Quantitative real-time PCR validated the decreased expression of myelination-associated genes in *Tet1* mutant. Data represent average transcript levels relative to control, after normalization as mean ± SEM for three independent experiments each performed in triplicates. *, $p<0.05$ compared to control by Student's *t* test.
(G) GSEA plots show the gene set of cell division that is downregulated in *Tet1* mutant.
(H) Quantitative real-time PCR validated the decreased expression of cell division and G2 M cell cycle related genes in *Tet1* cKO OPCs. Data represent average transcript levels relative to control, after normalization as mean ± SEM for three independent experiments each performed in triplicates. *, $p<0.05$ compared to control by Student's *t* test.
(I) GSEA plots show the gene set of calcium ion transmembrane transporter activity that is downregulated in *Tet1* mutant.
(J) Quantitative real-time PCR validated the decreased expression of calcium ion transmembrane transporter activity genes in *Tet1* cKO OPCs. Data represent average transcript levels relative to control, after normalization as mean ± SEM for three independent experiments each performed in triplicates. *, $p<0.05$ compared to control by Student's *t* test.
(K) GSEA plots show the gene set of regulation of neuron differentiation that is downregulated in *Tet1* mutant.
(L) Quantitative real-time PCR validated the decreased expression of neuron differentiation regulator genes in *Tet1* cKO OPCs. Data represent average transcript levels relative to control, after normalization ± SEM for three independent experiments each performed in triplicates. *, $p<0.05$ compared to control by Student's *t* test.

Figure 6. Correlation between DNA hydroxymethylation and gene transcription levels in oligodendrocytes from *Tet1* cKO mice
(A-B) Decreased fluorescence intensity of 5hmC in OLs from *Tet1* cKO brain. Representative image of 5hmC immunostaining in the corpus callosum of control and *Tet1* cKO mice. Note the attenuated level of 5hmC in $CC1^+$ cells in *Tet1* mutant as indicated by arrows (A). Quantification the fluorescence intensity revealed the significant decrease of 5hmC staining in $CC1^+$ cells from *Tet1* cKO brain. Data are mean ± SEM (n=3 animals each group) *, $p<0.05$ compared to control by Student's *t* test (B). Scale bar in A, 50μm.
(C-D) hMeDIP-seq was performed to compare the different DNA hydroxymethylation between control and *Tet1* cKO OPC cultures. Sequencing for each genotype was repeated once. Normalized 5hmC tag density distribution in OPCs from *Tet1* cKO and control groups (C). Heap map distribution of 5hmC peaks from ±5 kb of transcriptional start site (TSS) at all annotated genes in control and *Tet1* cKO OPCs (D).
(E) Diagram shows the correlation between differentially hydroxymethylated peaks at gene bodies and differentially expressed genes.
(F) Quadrant plot of differentially hydroxymethylated peaks at gene bodies and differentially expressed genes (*Tet1* cKO versus Control, $p<0.05$). The x axis refers to Log2 fold change of transcript level. The y axis indicated DNA hydroxymethylation difference. Horizontal and vertical (2 folds change) dashed lines identify genes in four quadrants. Marked genes in yellow quadrant (Lower-5hmC level and downregulated) are involved in the OL differentiation, cell division, calcium transporter and solute carrier.
(G) Representative 5hmC peaks in indicated genes derived from control (blue) and *Tet1* cKO

(orange) OPCs are shown. The upper row represents the gene body locations.

Figure 7. Abnormal $[Ca^{2+}]_i$ oscillations in OPCs from *Tet1* cKO mice and the effect of activating $[Ca^{2+}]_i$ on oligodendrocyte differentiation

(A-D) $[Ca^{2+}]_i$ oscillations following the treatment with Bay K 8644 in OPCs from control and *Tet1* cKO mice. Fluo-4 microfluorometry was used to compare intracellular $[Ca^{2+}]_i$ oscillations between groups. Representative serial images after addition of 10 μM Bay K 8644 in OPCs from control or *Tet1* cKO group (A). Note the delayed responding and weaker response in *Tet1* cKO groups. Representative traces of Fluo-4 intensity in OPCs from control and *Tet1* cKO mice, following application of agonist and antagonist for L-type voltage gated channel (Bay K8644 and Verapamil, respectively) (B). The average amplitude changes from Bay K 8644 stimulus was reduced in *Tet1* cKO groups. Data are mean ± SEM (n=82-87 cells, from three independent experiments) (C). The average value of Fluo-4 intensity rise slope after Bay K 8644 addition was reduced in *Tet1* cKO groups. Data are mean ± SEM (n=82-87 cells, from three independent cultures) (D).

(E-G) $[Ca^{2+}]_i$ oscillations following the treatment with ATP in OPCs from control and *Tet1* cKO mice. Representative traces of Fluo-4 intensity of OPCs from control and *Tet1* cKO mice, following application of ATP and antagonist for P2Y metabotropic receptor (MRS2179) (E). The average amplitude changes from ATP stimulus was reduced in *Tet1* cKO groups. Data are mean ± SEM (n=104-105 cells, from three independent cultures) (F). The average value of Fluo-4 intensity rise slope after ATP addition was reduced in *Tet1* cKO groups. Data are mean ± SEM (n=104-105 cells, from three independent cultures) (G). *, $p<0.05$, **, $p<0.01$, ***, $p<0.001$, by Student's *t* test.

(H-J) Bay K 8644 treatment promoted OL differentiation *in vitro* and rescue the deficiency of OL differentiation from *Tet1* cKO mice. Representative images of MBP immunostaining, indicating more differentiated OL in Bay K 8644 treated cell cultures in both groups (H). Quantification the percentage of MBP^+ cells among $Olig2^+$ cells after 3 days application of Bay K 8644. *, $p<0.05$ (I). Scar bar in H, 100 μm. Quantitative real-time PCR revealed the increased mRNA expression of myelin genes, *Cnp*, *Mbp* and *Plp*, with daily application of Bay K 8644 in OL cultures from both control and *Tet1* cKO groups, compared to blank in each group (J). Data represent average transcript levels relative to control, after normalization as mean ± SEM for three independent experiments each performed in triplicates. **, $p<0.01$, *, $p<0.05$ compared to control by two-way ANOVA.

(K-L) BrdU incorporation assay revealed fewer proliferating OPCs after application of 10 μM Bay K 8644. Representative images of BrdU and Olig2 staining for OPC cultures (K). Quantification the percentage of $BrdU^+$ among $Olig2^+$ cells. Data are mean ± SEM (n=3 different cultures each group) (L). *, $p<0.05$

Figure 8. Synaptic transmission deficits in *Tet1*-deficient animals

(A-C) Recordings of spontaneous EPSCs (sEPSCs) from the cortical pyramidal neurons of control and *Tet1* cKO cortex at P21. Representative recording traces of sEPSCs (A). Average frequency (B) and amplitude (C) of sEPSCs were calculated (n = 9 cells from two control and *Tet1* cKO mice, respectively). Error bars represent mean ± SEM. ***, $p < 0.001$ significance based on Student's *t* test.

(D-F) Recordings of miniature EPSCs (mEPSCs) from the cortical pyramidal neurons of control and *Tet1* cKO cortex at P22. Representative recording traces of mEPSCs (D). Average frequency (E) and amplitude (F) of mEPSCs were calculated (n = 10 cells from two control mice and n=12 cells from two *Tet1* cKO mice, respectively.) Data represent mean ± SEM. **, $p < 0.01$ significance based on Student's *t* test.

(G-H) Expression of presynaptic markers in P21 *Tet1* cKO mice. Representative images of immunostaining for Synaptophysin-1 and excitatory presynaptic terminal marker, vGluT1, in M2 cortex of control and *Tet1* cKO mice. Neurons were co-labeled with MAP2. Scale bar, 10 μm (G). Quantification the puncta staining of pre- and post- synaptic markers using Imaris software. Data represent mean ± SEM. **, $p < 0.01$ significance based on Student's *t* test (H).

(I) Expression of Synaptophysin, vGluT1, Homer1, PSD95 in control (C) and *Tet1* mutant (M) cortex

was analyzed by Western blot. β-Tubulin was used as loading control.
(J) Histogram showed fold changes of synaptic markers measured by densitometry in *Tet1* mutant against control after normalization with β-Tubulin. *, $p<0.05$ compared to control by Student's *t* test (n=3 animals each group).

Supplementary figure legends:

Figure S1. Examples OL lineage specific genes that showed exclusive 5hmC peaks in promoter-TSS region in OPC

(A) Column diagrams show the expression of representative genes in different OL stage. Genes with OPC-specific 5hmC peak that are exclusively expressed in OL lineage. The diagrams are downloaded from http://web.stanford.edu/group/barres_lab/brain_ rnaseq.html.

(B) Snapshots of 5hmC profiles for representative genes from NPC and OPC. Genomic region encompassing promoter-TSS were compared between groups. Genes highly expressed in OPC, immature OL (iOL), mature OL (OL) were shown. *Cspg* (chondroitin sulfate proteoglycan 4), *Slc22a3* (solute carrier family 22 member 3), *Atp2b3* (ATPase plasma membrane Ca^{2+} transporting 3), *Tmem141* (transmembrane protein 141), *Kndc1* (kinase non-catalytic C-lobe domain containing 1), *Ptprd* (protein tyrosine phosphatase, receptor type D), *Mag* (myelin-associated glycoprotein), *Cdc42ep2* (CDC42 effector protein 2), *Elovl7* (elongation of very long chain fatty acids protein 7).

Figure S2. Deletion of *Tet3* showed no significant effects on the process of myelination

(A) Schematic diagram shows Cre-mediated excision of floxed Tet3 exons encoding the catalytic center in dioxygenase activity, modified from Gu et al., 2011.

(B) Representative image of MBP immunostaining of P16 brain from control and *Tet3* cKO mice. Scale bar, 100μm.

(C) Western blot assay for MBP expression revealed no difference at P16 between control (C) and *Tet3* mutant (M), with β-actin as loading control.

(D) Western blot assay for Olig2 expression revealed no difference between control (C) and *Tet3* mutant (M), with β-actin as loading control.

(E-F) Co-labeling of Sox10 and CC1 revealed no difference between control and *Tet3* cKO P7 brain. Representative images of different region of Sox10 and CC1 immunostaining from control and *Tet3* cKO brains (E). Quantification of Sox10 and CC1 double positive cells revealed comparable cell numbers between two groups. Data are mean±SEM (n=3 animals each group) (F). Scale bar in E, 100μm.

(G-H) Immunostaining and quantification of Sox10 positive cells revealed no difference between control and *Tet3* cKO P14 brain. Data are mean±SEM (n=3 animals each group). Scale bar in G, 100μm.

Figure S3. Comparable OL differentiation and myelination in *Tet1* heterozygous control, Cre control and wild type mice.

(A) Representative immunostaining of mature OL marker CC1, OL lineage marker Sox10, and myelin protein MBP in P14 mice from indicated mice. Scale bar, 50 μm.

(B) Quantification of $CC1^+$ cell in defined areas among groups.

Figure S4. Ablation of *Tet1* in OL lineage cells results in stage dependent OL differentiation deficiencies

(A) Representative immunostaining of CC1, Sox10 and MBP at P21 and 2M. Note the comparable number of $CC1^+$ cells and MBP intensity in 2M. Scale bar, 50 μm.

(B) Expression of MBP in control (C) and *Tet1* mutant (M) brains was analyzed by Western blot. β-actin was used as loading control. Histogram showed fold changes measured by densitometry in *Tet1* mutant against control after normalization with β-actin. *, $p<0.05$ compared to control by Student's *t* test (n=3 animals each group).

(C-D) Expression of TET1 in $Sox10^+$ OLs from two-month old *Tet1* cKO mice. Representative immunostaining images revealed the low expression of TET1 in Sox10 positive cells in corpus collosum from both groups. Arrows indicate TET1/Sox10 double positive cells in both groups (C). Scale bar, 20 μm. Quantification the percentage of TET1/Sox10 double positive cells among Sox10

positive oligodendrocytes. Data are mean±SEM (n=3 animals each group). **, $p<0.01$ compared to control by Student's *t* test (D).
(E-F) Loss of TET1 results in less OLs from embryonic stage. Representative images of Olig2 staining at E15.5 from both groups (E). Scale bar, 100 μm. Quantification of Olig2 positive cells in cortex from E13.5 and E15.5 mice (F). *, $p<0.05$ compared to control by Student's *t* test (n=3 animals each group).

Figure S5. Normal myelination in spinal cord of *Tet1* cKO mice.
(A-C) The number of mature oligodendrocytes was reduced in P8 spinal cord from *Tet1* cKO mice. Representative images of Olig2/CC1 co-immunostaining in the spinal cord of *Tet1* mutant (A). Scale bar, 100μm. Quantification of $Olig2^+$ cells in defined field of spinal cord revealed comparable oligodendrocyte numbers between *Tet1* cKO and control mice. Data are mean±SEM (n=3 animals each group) (B). Quantification of $CC1^+$ cells in defined field of spinal cord showed significant decrease in *Tet1* cKO mice. Data are mean±SEM (n=3 animals each group). *, $p<0.05$ (C).
(D) Representative images of MBP immunostaining in spinal cord from P8 *Tet1* cKO mice. Note the similar staining intensity in both groups. Scale bar, 100μm.
(E-F) Ultrastructure of myelin sheaths of P14 spinal cord was comparable between control and *Tet1* cKO mice. Representative electron micrographs of spinal cord from control and *Tet1* cKO mice (E). G ratio of myelin was similar between two groups (F). Scale bar in E, 2 μm.

Figure S6. Hypomyelination in *Tet1* cKO young mice caused deficits in the transduction of compound action potential (CAP)
(A) Representative CAP series from optic nerves of control and *Tet1* cKO mice elicited by square voltage pulses with varied amplitudes.
(B) Evoked CAP amplitudes of the 2^{nd} peak (maximal) from control and *Tet1* cKO mice were plotted versus stimulus currents.
(C) Total CAP area vs. stimulus current illustrating the significant decrease of CAP area in *Tet1* cKO mice at all stimulus intensity compared to control. Data are mean±SEM (n=10 nerves each group).

Figure S7. Normal apoptosis and more proliferating OL precursor cells in *Tet1* cKO brain
(A-B) No alterations in the apoptosis of OL lineage cells were observed in *Tet1* cKO mice as revealed by TUNEL/Olig2 double staining. Olig2 immunostaining after TUNEL staining revealed similar number of apoptotic cells between two groups at P1 and the double labeling cells can be hardly detected (A). Quantification of TUNEL positive cells from E14.5 to P1 stage revealed no overall difference between two groups. Data are mean±SEM (n=3 animals each group) (B). Scale bar in A, 50 μm.
(C-D) More proliferating OPCs was observed in *Tet1* cKO mice. Representative images of Ki67/Sox10 double immunostaining in different regions as indicated from P1 control or *Tet1* cKO mice (C). Quantification of the proportion of $Ki67^+$ cells within $Sox10^+$ population. Data are mean ± SEM (n=3 animals each group) (D). *, $p<0.05$ compared to control by Student's *t* test. Scale bar in C, 100 μm.

Figure S8. Normal development of astrocyte and neuron in *Tet1* cKO mice.
(A-B) Normal neuronal development in *Tet1* cKO mice. A Western blot assay revealed that the expression of DCX, marker for newly generated neuron, in *Tet1* cKO embryonic brain was comparable to that of control at different developmental stages. Tubulin was included as loading control (A). Immunostaining of NeuN in P1 brain showed similar expression in both groups (B). Scar bar, 100 μm.
(C-D) Astrocytes identified by ALDHL1 immunostaining in P1 brain showed similar number in defined area between control and *Tet1* cKO mice. Immunostaining for ALDHL1 in P1 brain S1

cortex (C). Quantification of ALDHL1$^+$ cells revealed no difference between two groups. Data are mean ± SEM (n=3 animals each group) (D). Scale bar in C, 100 μm.
(E) Western blot assay for the expression of ALDHL1 and NeuN, markers for astrocyte and neuron respectively, in the brain samples from postnatal control (C) and *Tet1* cKO (M) mice. β-actin was used as loading control.

Figure S9. Deficiency of OPC differentiation in *Tet1* OPC-iKO mice
(A) Diagram showing TAM administration to induce the Cre recombination in *Tet1* OPC-iKO (*NG2-CreER*^{T}:*Tet1*$^{flox/flox}$) mice.
(B-C) Reduced expression of TET1 in Sox10$^+$ OLs from *Tet1*-iKO mice. Representative immunostaining images revealed the decreased expression of TET1 in Sox10 positive cells in P7 corpus collosum from *Tet1*-iKO mice. Arrows indicate Sox10$^+$ cells that show reduced level of TET1 in *Tet1*-iKO groups (B). Scale bar, 20 μm. Quantification the percentage of TET1/Sox10 double positive cells among Sox10 positive oligodendrocytes in P7 corpus collosum. Data are mean±SEM (n=3 animals each group). **, p<0.01 compared to control by Student's t test (C).
(D-F) The number of mature oligodendrocytes and MBP expression was significantly decreased in *Tet1*-iKO mice. Representative images of CC1/Sox10 and MBP immunostaining in the corpus callosum of P7 and P14 animals as indicated (D). Quantification the density of CC1 positive cells at P14 (E) and MBP positive cells at P7 (F), respectively. *, p<0.05, ***, p<0.001 compared to control by Student's t test (n=3 animals each group). Scale bar in D, 100μm.

Figure S10. Characterization of 5hmC peaks in the genome of OPC from *Tet1* cKO mice.
(A) The number of total 5hmC peaks from hMeDIP-seq was significantly reduced in *Tet1* cKO groups.
(B) Genomic distribution of 5hmC in OPCs from control and *Tet1* cKO mice.
(C) Proportion of differentially hydroxymethylated regions with different CpG densities. Note that DhMRs is enriched at genomic regions with low-density CpG dinucleotides.
(D) Diagram shows the overlap between differentially hydroxymethylated genes at promoters and differentially expressed genes.
(E) Quadrant plot of differentially hydroxymethylated genes at promoters and differentially expressed genes (*Tet1* cKO versus Control, p<0.05)**.** The x axis refers to fold change of transcript level. The y axis indicated DNA hydroxymethylation difference. Horizontal and vertical (2 folds change) dashed lines identify genes in four quadrants.
(F) Representative 5hmC peaks of calcium transporter genes in oligodendrocytes derived from control (blue) and *Tet1* cKO (orange) mice. The upper row represents the gene bodies located in this particular region of the genome.

Figure S11. Decreased expression and secretion of GDNF from *Tet1* cKO OPC cultures
(A) Expression of GDNF in control (C) and *Tet1* mutant (M) OPC cultures was analyzed by Western blot. β-actin was used as loading control. Histogram showed fold changes measured by densitometry in *Tet1* cKO against control after normalization with β-actin. ***, p<0.001 compared to control by Student's t test (n=3 different cultures each group).
(B) Concentration of GDNF from the supernatant of purified OPC cultures as tested by ELISA assay. **, p<0.001 compared to control by Student's t test (n=3 different cultures each group).
(C-E) Flow cytometry revealed less percentage of cells in S and G2/M phase after Bay K 8644 treatment. Representative diagram of flow cytometry with PI DNA staining in purified OPCs from DMSO (control vehicle, C) and Ca^{2+} channel agonist Bay K 8644 (D). Quantification the percentage of cells in each phase (E). The experiments were repeated from three individual cultures and the data are mean ± SEM. *, p<0.05 compared to control vehicle by Student's t test.

Figure S12. Ultrastructure of synapse and expression of synaptic markers in *Tet1* mutant

(A) Representative images of ultrastructure for synapses in M2 cortex of P21 control and *Tet1* cKO mice. Red arrows indicated synapse in both groups. Scale bar, 200 nm.
(B) Quantification the density of synapses between groups. No obvious difference was observed.
(C) Representative images of immunostaining for the excitatory presynaptic marker, vGlut2, and postsynaptic marker, Homer1, in the M2 cortex of control and *Tet1* cKO mice at P21. Scale bar, 20 μm.

Table S1: Transcriptome changes in OPCs from *Tet1* cKO mice.

Movie S1: $[Ca^{2+}]_i$ oscillations recorded from Bay K 8644 stimulated control OPCs in culture as reveal by Fluo4.

MovieS2: $[Ca^{2+}]_i$ oscillations recorded from Bay K 8644 stimulated *Tet1* cKO OPCs in culture as reveal by Fluo4.

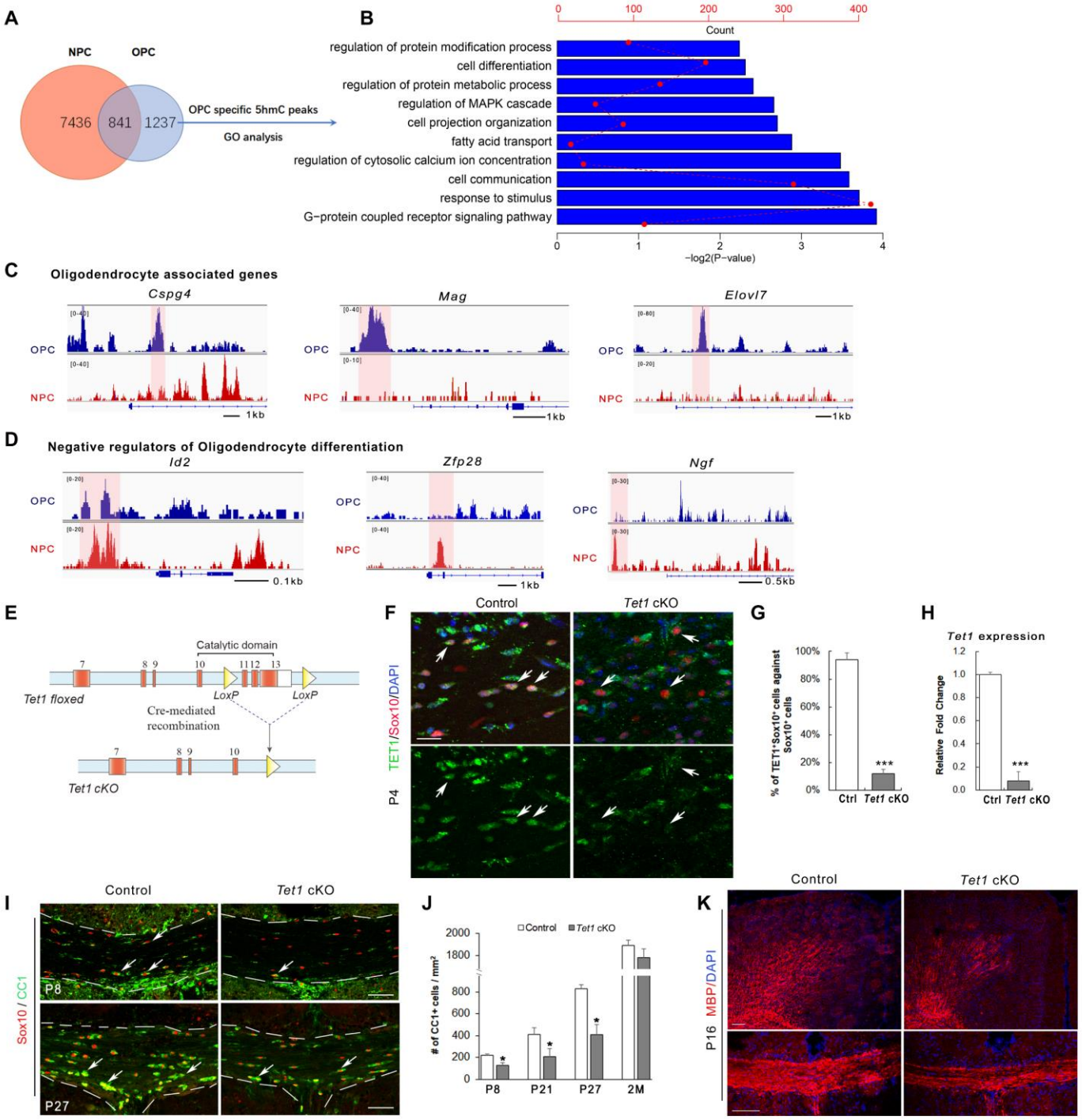
A
NPC
OPC
7436
841
1237
OPC specific 5hmC peaks
GO analysis
B
Count
regulation of protein modification process
cell differentiation
regulation of protein metabolic process
regulation of MAPK cascade
cell projection organization
fatty acid transport
regulation of cytosolic calcium ion concentration
cell communication
response to stimulus
G−protein coupled receptor signaling pathway
−log2(P−value)
C
Oligodendrocyte associated genes
Cspg4
Mag
Elovl7
OPC
NPC
1kb
D
Negative regulators of Oligodendrocyte differentiation
Id2
Zfp28
Ngf
0.1kb
0.5kb
E
Catalytic domain
Tet1 floxed
LoxP
Cre-mediated recombination
Tet1 cKO
F
Control
Tet1 cKO
TET1/Sox10/DAPI
P4
G
% of TET1+Sox10+ cells against Sox10+ cells
Ctrl
H
Tet1 expression
Relative Fold Change
I
Sox10 / CC1
P8
P27
J
# of CC1+ cells / mm²
P8
P21
P27
2M
K
P16
MBP/DAPI

Figure 1

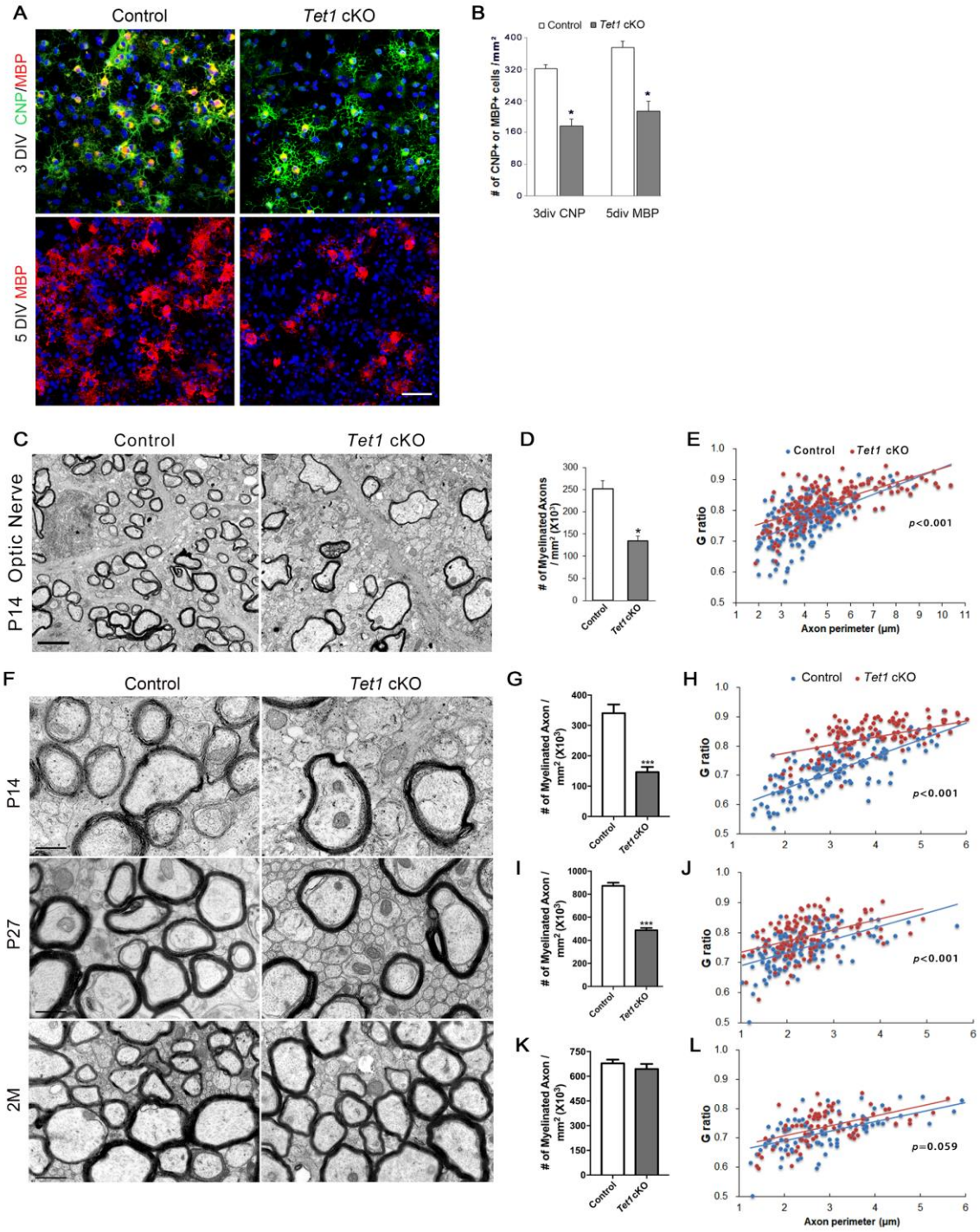
A
Control
Tet1 cKO
3 DIV CNP/MBP
5 DIV MBP
B
Control
Tet1 cKO
# of CNP+ or MBP+ cells /mm²
3div CNP
5div MBP
C
Control
Tet1 cKO
P14 Optic Nerve
D
# of Myelinated Axons / mm² (X10²)
Control
Tet1cKO
E
Control
Tet1 cKO
G ratio
p<0.001
Axon perimeter (μm)
F
Control
Tet1 cKO
P14
P27
2M
G
# of Myelinated Axon / mm² (X10³)
H
p<0.001
I
J
p<0.001
K
L
p=0.059
Axon perimeter (μm)

Figure 2

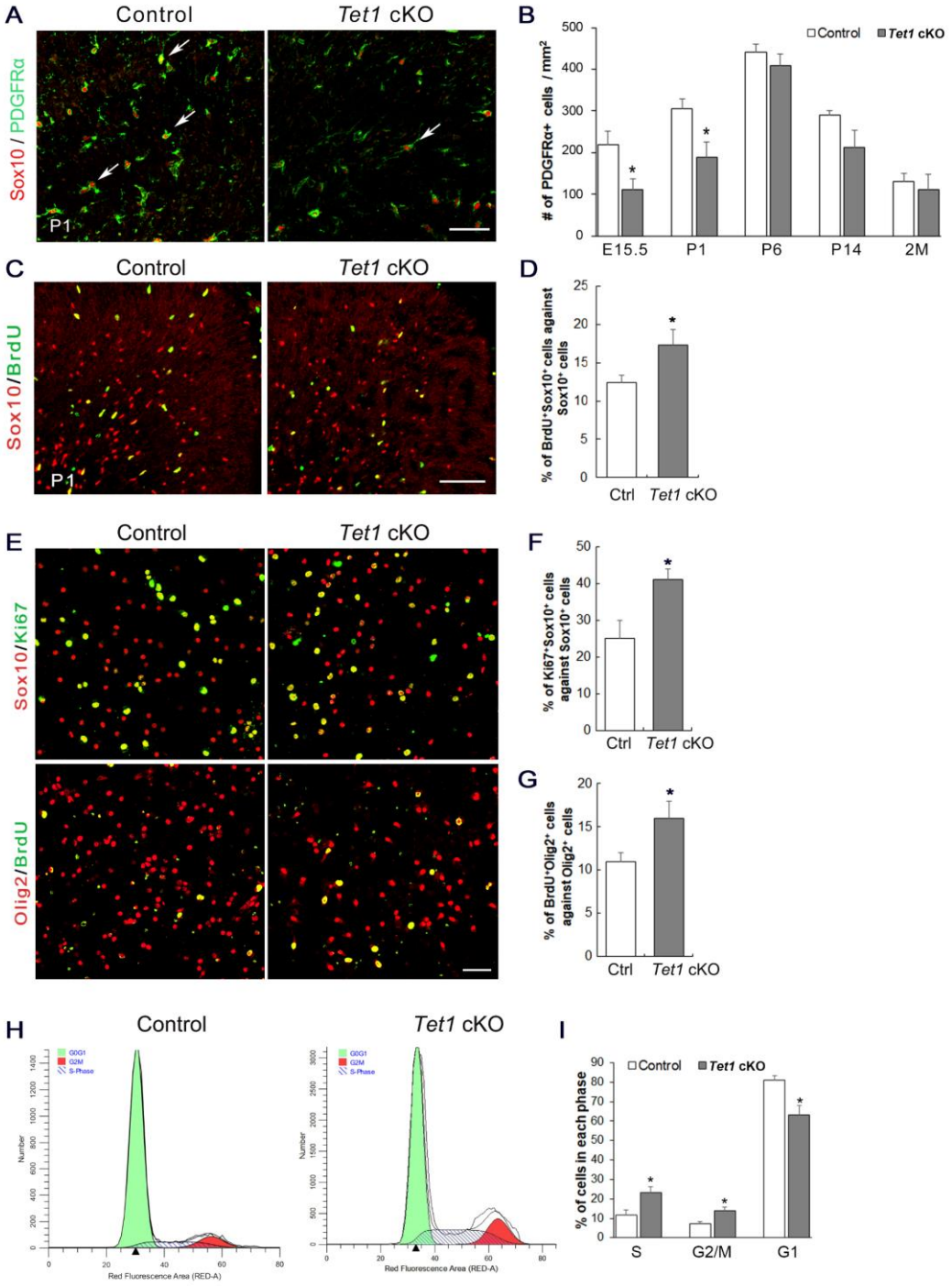
A
Control
Tet1 cKO
Sox10 / PDGFRα
P1
B
Control
Tet1 cKO
# of PDGFRα+ cells / mm²
E15.5
P1
P6
P14
2M
C
Control
Tet1 cKO
Sox10/BrdU
P1
D
% of BrdU+Sox10+ cells against Sox10+ cells
Ctrl
Tet1 cKO
E
Control
Tet1 cKO
Sox10/Ki67
Olig2/BrdU
F
% of Ki67+Sox10+ cells against Sox10+ cells
Ctrl
Tet1 cKO
G
% of BrdU+Olig2+ cells against Olig2+ cells
Ctrl
Tet1 cKO
H
Control
Tet1 cKO
G0G1
G2M
S-Phase
Number
Red Fluorescence Area (RED-A)
I
Control
Tet1 cKO
% of cells in each phase
S
G2/M
G1

Figure 3

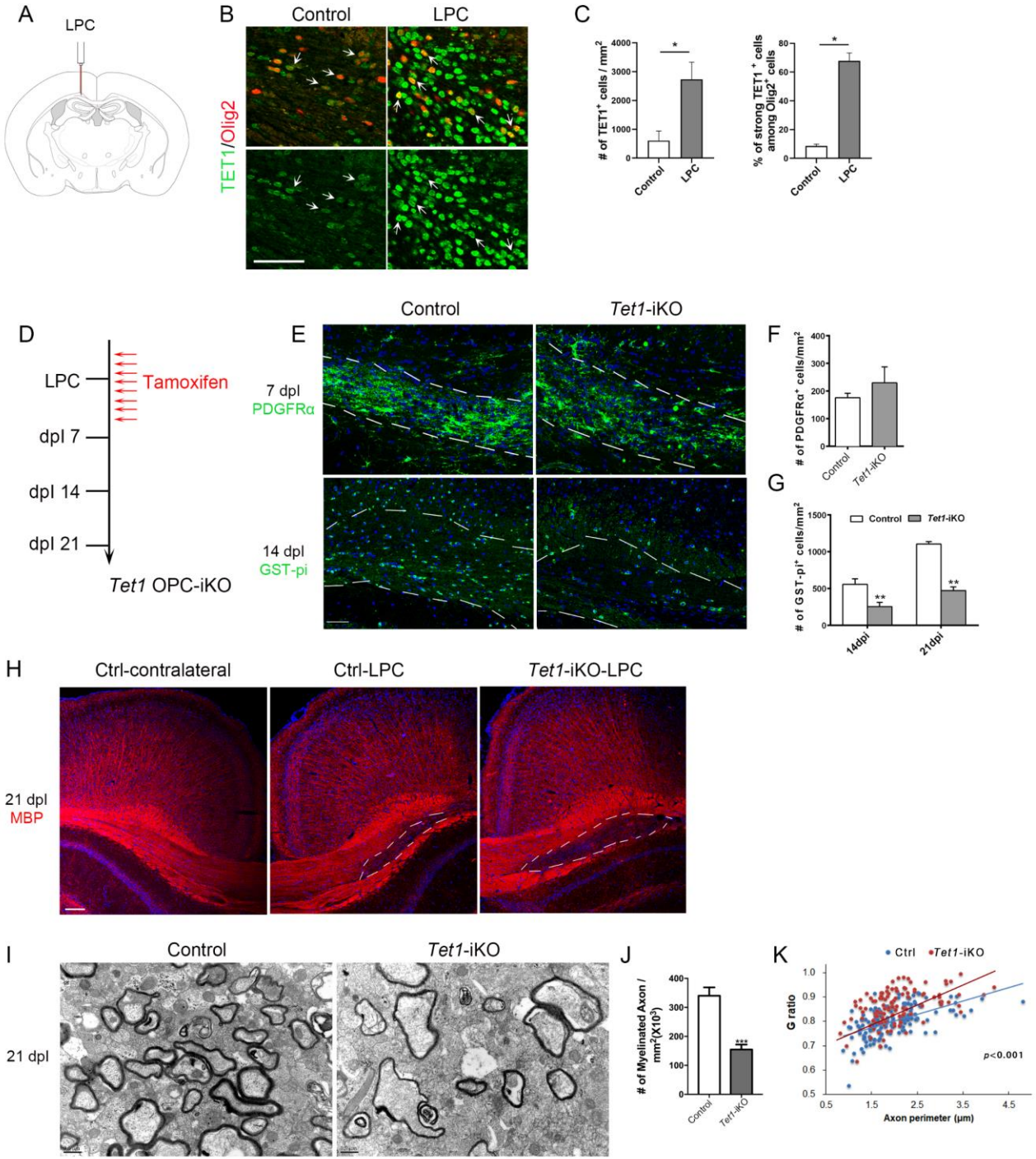
A
LPC
B
Control
LPC
TET1/Olig2
C
# of TET1+ cells / mm2
% of strong TET1+ cells among Olig2+ cells
Control
LPC
D
LPC
Tamoxifen
dpI 7
dpI 14
dpI 21
Tet1 OPC-iKO
E
Control
Tet1-iKO
7 dpI
PDGFRα
14 dpI
GST-pi
F
# of PDGFRα+ cells/mm2
G
# of GST-pi+ cells/mm2
14dpI
21dpI
H
Ctrl-contralateral
Ctrl-LPC
Tet1-iKO-LPC
21 dpI
MBP
I
Control
Tet1-iKO
21 dpI
J
# of Myelinated Axon / mm2(X10³)
K
Ctrl
Tet1-iKO
G ratio
p<0.001
Axon perimeter (μm)

Figure 4

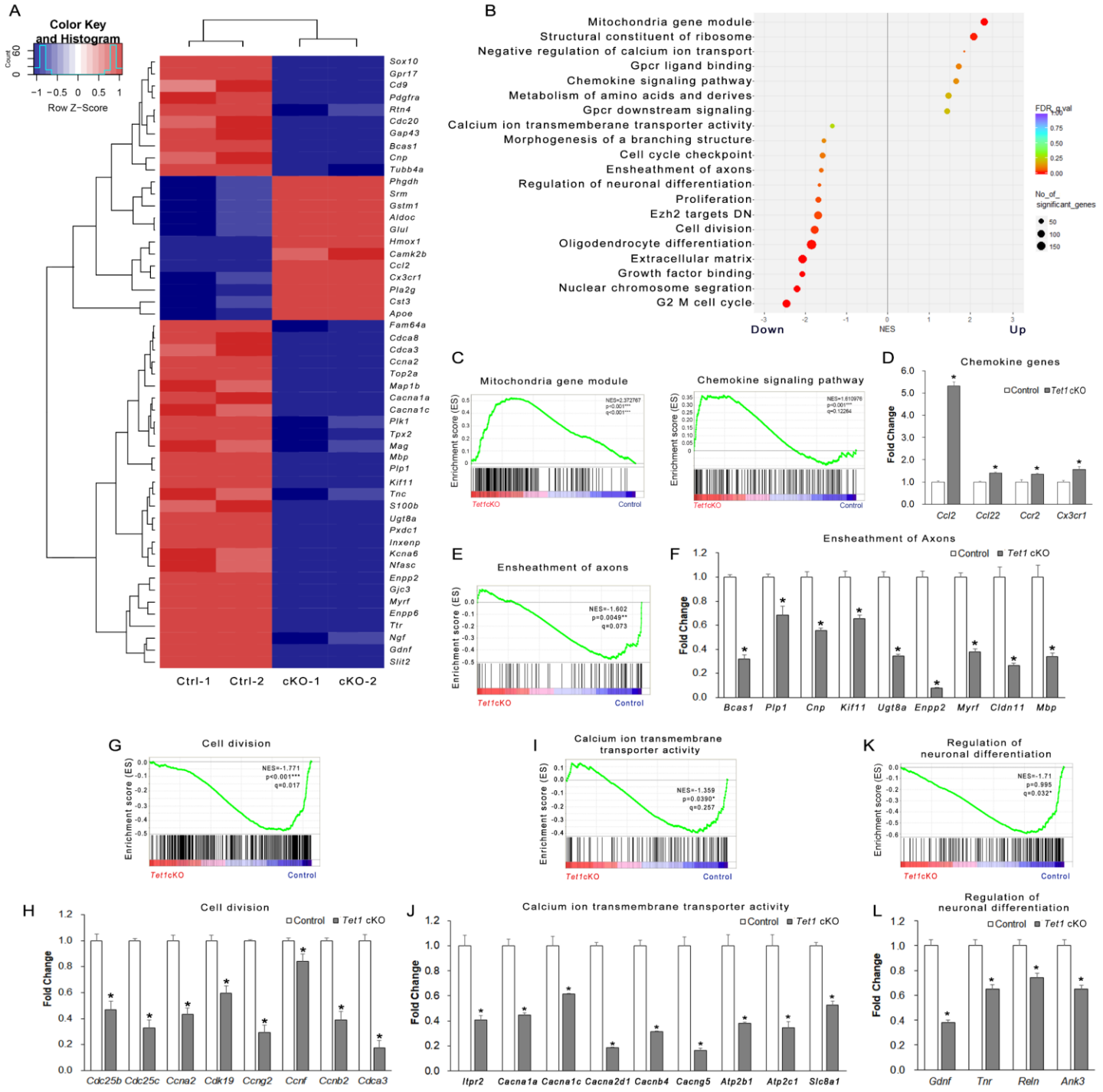
A
Color Key and Histogram
Count
Row Z-Score
Sox10
Gpr17
Cd9
Pdgfra
Rtn4
Cdc20
Gap43
Bcas1
Cnp
Tubb4a
Phgdh
Srm
Gstm1
Aldoc
Glul
Hmox1
Camk2b
Ccl2
Cx3cr1
Pla2g
Cst3
Apoe
Fam64a
Cdca8
Cdca3
Ccna2
Top2a
Map1b
Cacna1a
Cacna1c
Plk1
Tpx2
Mag
Mbp
Plp1
Kif11
Tnc
S100b
Ugt8a
Pxdc1
Inxenp
Kcna6
Nfasc
Enpp2
Gjc3
Myrf
Enpp6
Ttr
Ngf
Gdnf
Slit2
Ctrl-1
Ctrl-2
cKO-1
cKO-2
B
Mitochondria gene module
Structural constituent of ribosome
Negative regulation of calcium ion transport
Gpcr ligand binding
Chemokine signaling pathway
Metabolism of amino acids and derives
Gpcr downstream signaling
Calcium ion transmemberane transporter activity
Morphogenesis of a branching structure
Cell cycle checkpoint
Ensheathment of axons
Regulation of neuronal differentiation
Proliferation
Ezh2 targets DN
Cell division
Oligodendrocyte differentiation
Extracellular matrix
Growth factor binding
Nuclear chromosome segration
G2 M cell cycle
FDR_q.val
No_of_ significant_genes
Down
NES
Up
C
Mitochondria gene module
Chemokine signaling pathway
Enrichment score (ES)
Tet1cKO
Control
D
Chemokine genes
Control
Tet1 cKO
Fold Change
Ccl2
Ccl22
Ccr2
Cx3cr1
E
Ensheathment of axons
NES=-1.602
p=0.0049**
q=0.073
F
Ensheathment of Axons
Bcas1
Plp1
Cnp
Kif11
Ugt8a
Enpp2
Myrf
Cldn11
Mbp
G
Cell division
NES=-1.771
p<0.001***
q=0.017
I
Calcium ion transmembrane transporter activity
NES=-1.359
p=0.0390*
q=0.257
K
Regulation of neuronal differentiation
NES=-1.71
p=0.995
q=0.032*
H
Cell division
Cdc25b
Cdc25c
Ccna2
Cdk19
Ccng2
Ccnf
Ccnb2
Cdca3
J
Calcium ion transmembrane transporter activity
Itpr2
Cacna1a
Cacna1c
Cacna2d1
Cacnb4
Cacng5
Atp2b1
Atp2c1
Slc8a1
L
Regulation of neuronal differentiation
Gdnf
Tnr
Reln
Ank3

Figure 5

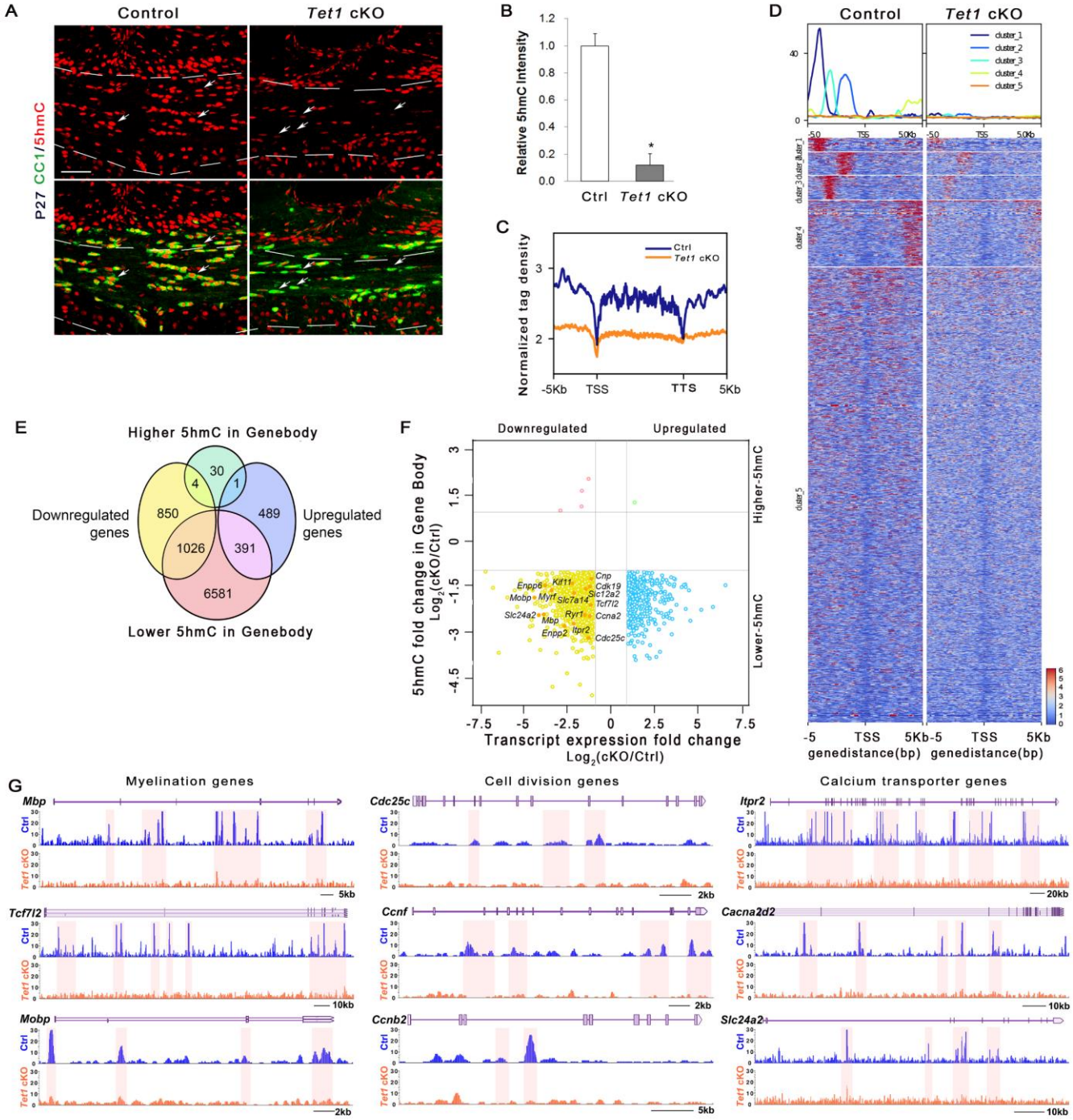
A
Control
Tet1 cKO
P27 CC1/5hmC
B
Relative 5hmC Intensity
Ctrl
Tet1 cKO
C
Normalized tag density
Ctrl
Tet1 cKO
-5Kb
TSS
TTS
5Kb
D
Control
Tet1 cKO
cluster_1
cluster_2
cluster_3
cluster_4
cluster_5
genedistance(bp)
E
Higher 5hmC in Genebody
Downregulated genes
Upregulated genes
Lower 5hmC in Genebody
30
4
1
850
489
1026
391
6581
F
Downregulated
Upregulated
Higher-5hmC
Lower-5hmC
5hmC fold change in Gene Body
Log2(cKO/Ctrl)
Transcript expression fold change
Log2(cKO/Ctrl)
Enpp6
Kif11
Mobp
Myrf
Slc7a14
Slc24a2
Mbp
Ryr1
Enpp2
Itpr2
Cnp
Cdk19
Slc12a2
Tcf7l2
Ccna2
Cdc25c
G
Myelination genes
Cell division genes
Calcium transporter genes
Mbp
Cdc25c
Itpr2
Tcf7l2
Ccnf
Cacna2d2
Mobp
Ccnb2
Slc24a2
Ctrl
Tet1 cKO

Figure 6

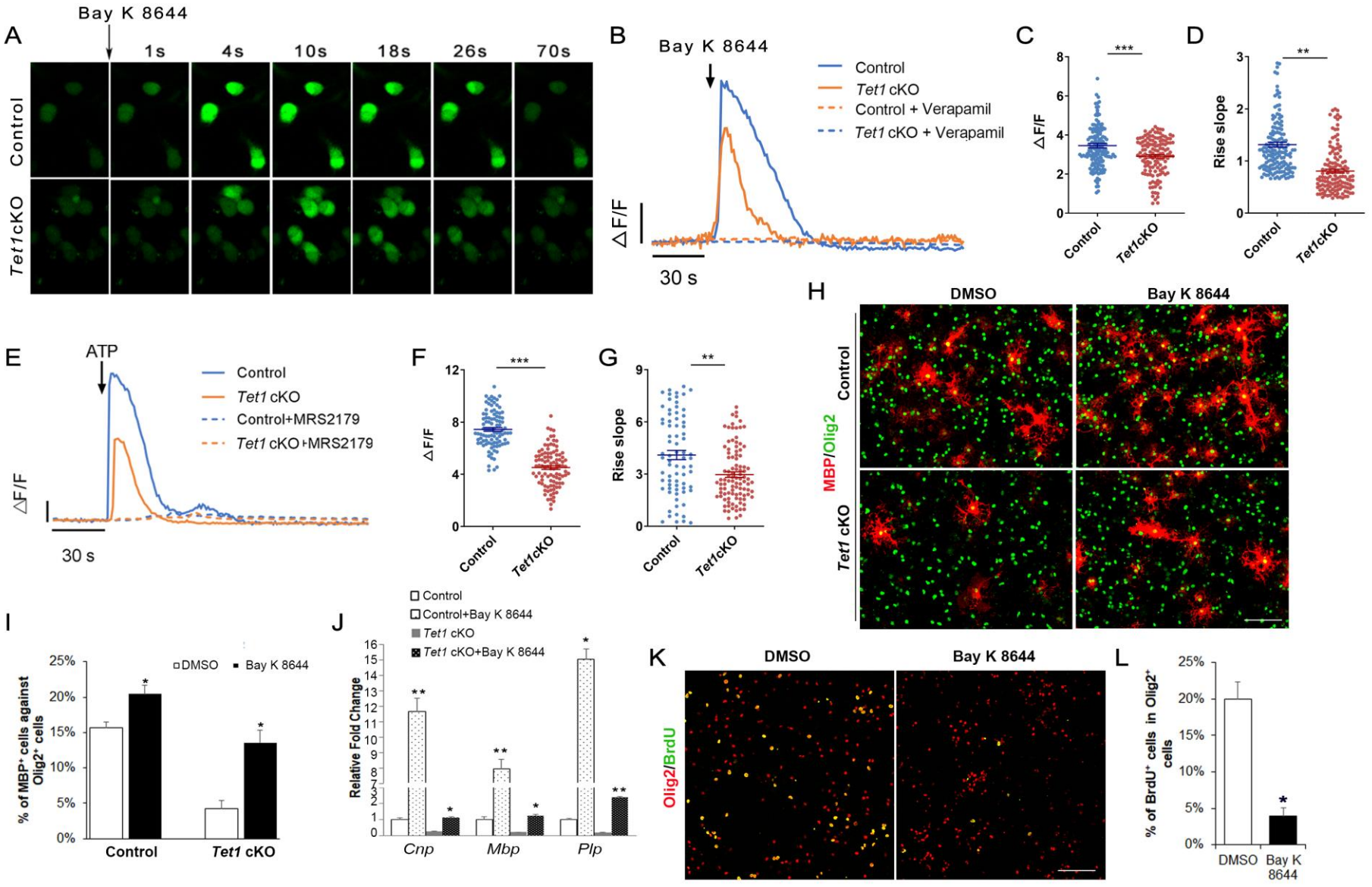
A
Bay K 8644
1s
4s
10s
18s
26s
70s
Control
Tet1cKO
B
Bay K 8644
Control
Tet1 cKO
Control + Verapamil
Tet1 cKO + Verapamil
ΔF/F
30 s
C
***
ΔF/F
Control
Tet1cKO
D
**
Rise slope
Control
Tet1cKO
E
ATP
Control
Tet1 cKO
Control+MRS2179
Tet1 cKO+MRS2179
ΔF/F
30 s
F
***
ΔF/F
Control
Tet1cKO
G
**
Rise slope
Control
Tet1cKO
H
DMSO
Bay K 8644
Control
Tet1 cKO
MBP/Olig2
I
DMSO
Bay K 8644
% of MBP+ cells against Olig2+ cells
Control
Tet1 cKO
J
Control
Control+Bay K 8644
Tet1 cKO
Tet1 cKO+Bay K 8644
Relative Fold Change
Cnp
Mbp
Plp
K
DMSO
Bay K 8644
Olig2/BrdU
L
% of BrdU+ cells in Olig2+ cells
DMSO
Bay K 8644

Figure 7

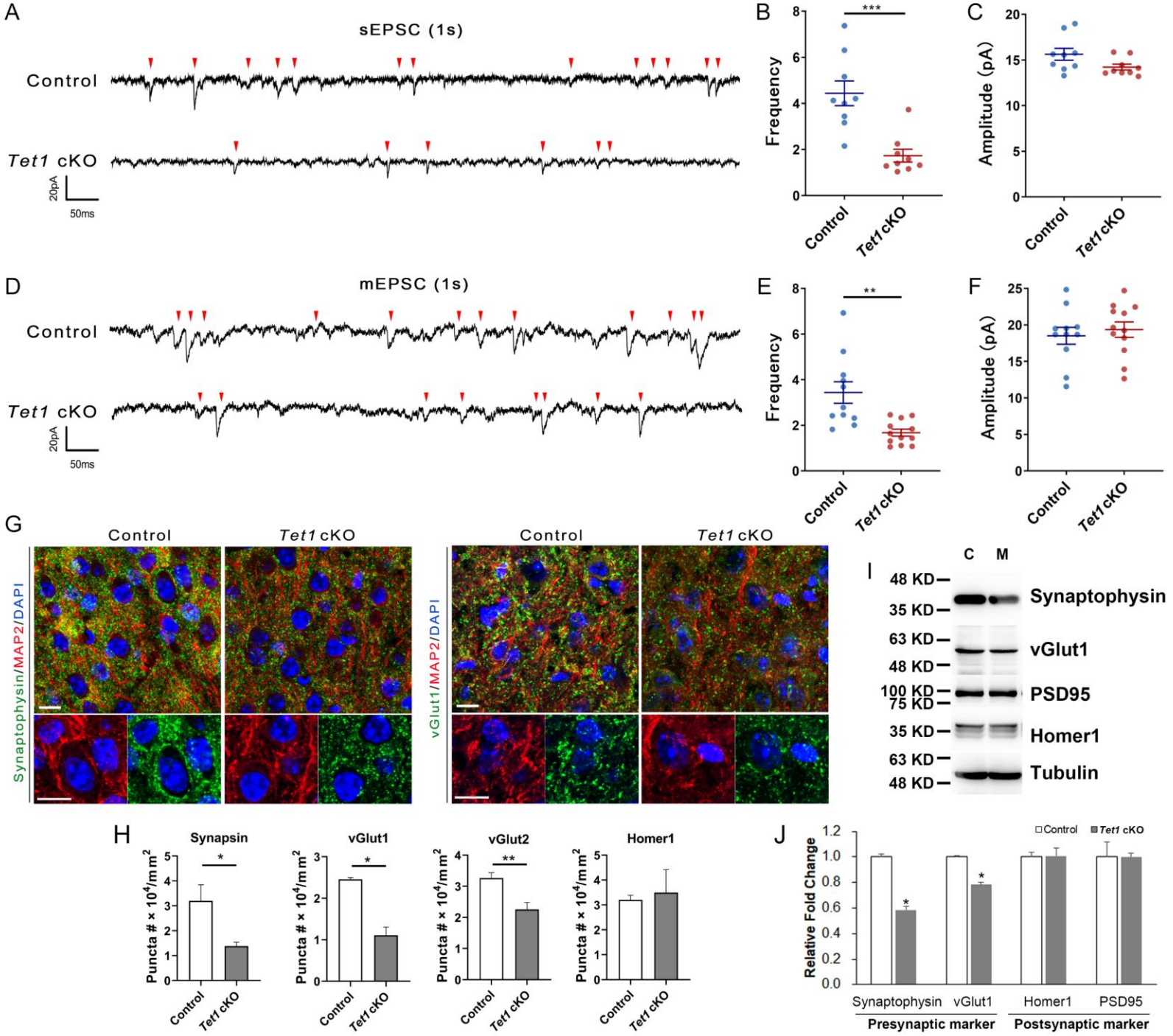
A
sEPSC (1s)
Control
Tet1 cKO
20pA
50ms
B
***
Frequency
Control
Tet1cKO
C
Amplitude (pA)
Control
Tet1cKO
D
mEPSC (1s)
Control
Tet1 cKO
20pA
50ms
E
**
Frequency
Control
Tet1cKO
F
Amplitude (pA)
Control
Tet1cKO
G
Control
Tet1 cKO
Synaptophysin/MAP2/DAPI
Control
Tet1 cKO
vGlut1/MAP2/DAPI
I
C
M
48 KD
35 KD
Synaptophysin
63 KD
48 KD
vGlut1
100 KD
75 KD
PSD95
35 KD
Homer1
63 KD
48 KD
Tubulin
H
Synapsin
vGlut1
vGlut2
Homer1
Puncta # × 10^4/mm^2
Control
Tet1cKO
J
Control
Tet1 cKO
Relative Fold Change
Synaptophysin
vGlut1
Homer1
PSD95
Presynaptic marker
Postsynaptic marker

Figure 8

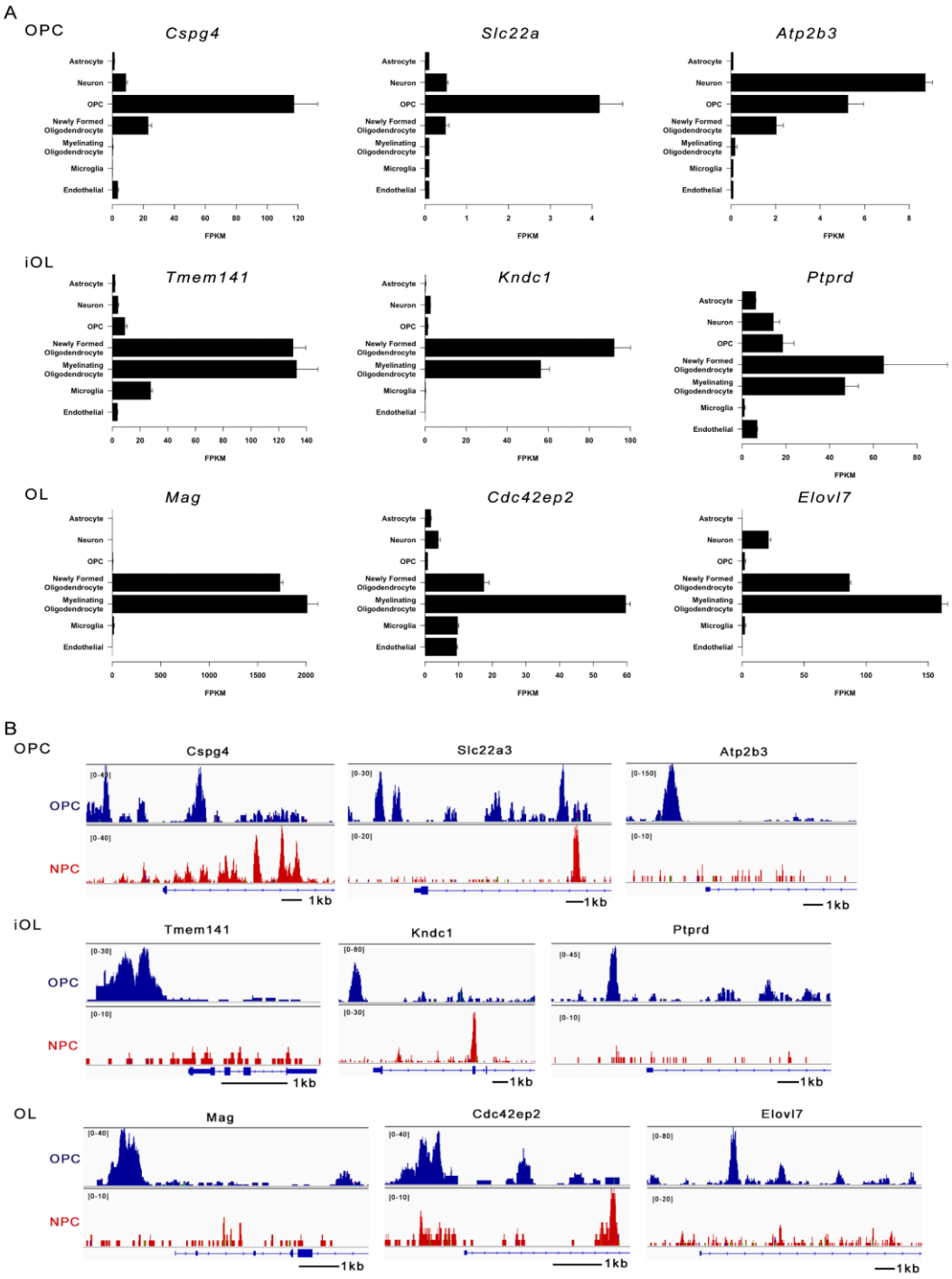
A
OPC
Cspg4
Slc22a
Atp2b3
iOL
Tmem141
Kndc1
Ptprd
OL
Mag
Cdc42ep2
Elovl7
Astrocyte
Neuron
OPC
Newly Formed Oligodendrocyte
Myelinating Oligodendrocyte
Microglia
Endothelial
FPKM
B
OPC
Cspg4
Slc22a3
Atp2b3
iOL
Tmem141
Kndc1
Ptprd
OL
Mag
Cdc42ep2
Elovl7
OPC
NPC
1kb

Figure S1

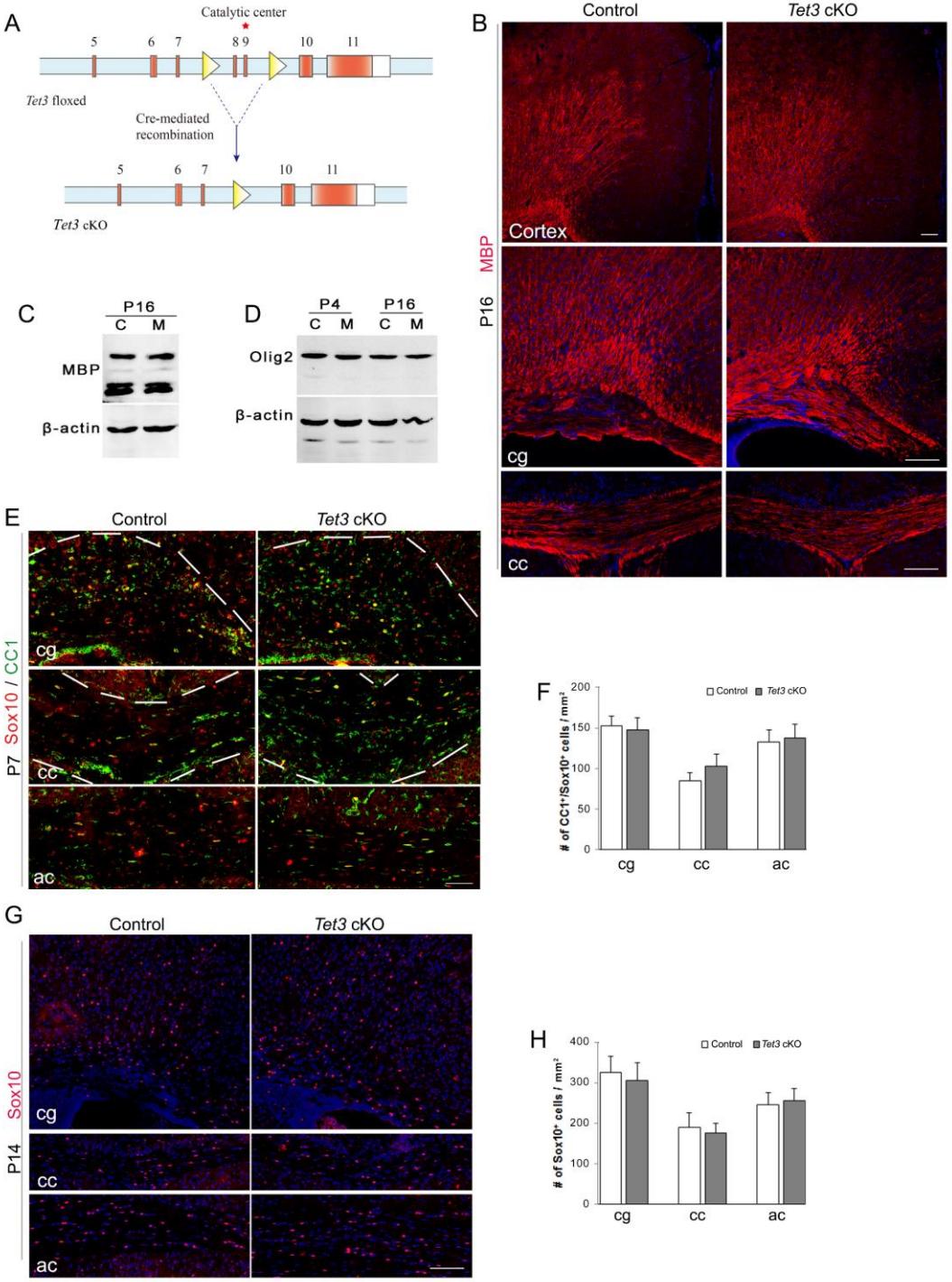
A
Catalytic center
5 6 7 8 9 10 11
Tet3 floxed
Cre-mediated recombination
5 6 7 10 11
Tet3 cKO
B
Control
Tet3 cKO
MBP
P16
Cortex
cg
cc
C
P16
C M
MBP
β-actin
D
P4 P16
C M C M
Olig2
β-actin
E
Control
Tet3 cKO
P7 Sox10 / CC1
cg
cc
ac
F
Control Tet3 cKO
# of CC1+/Sox10+ cells / mm²
200
150
100
50
0
cg cc ac
G
Control
Tet3 cKO
P14 Sox10
cg
cc
ac
H
Control Tet3 cKO
# of Sox10+ cells / mm²
400
300
200
100
0
cg cc ac

Figure S2

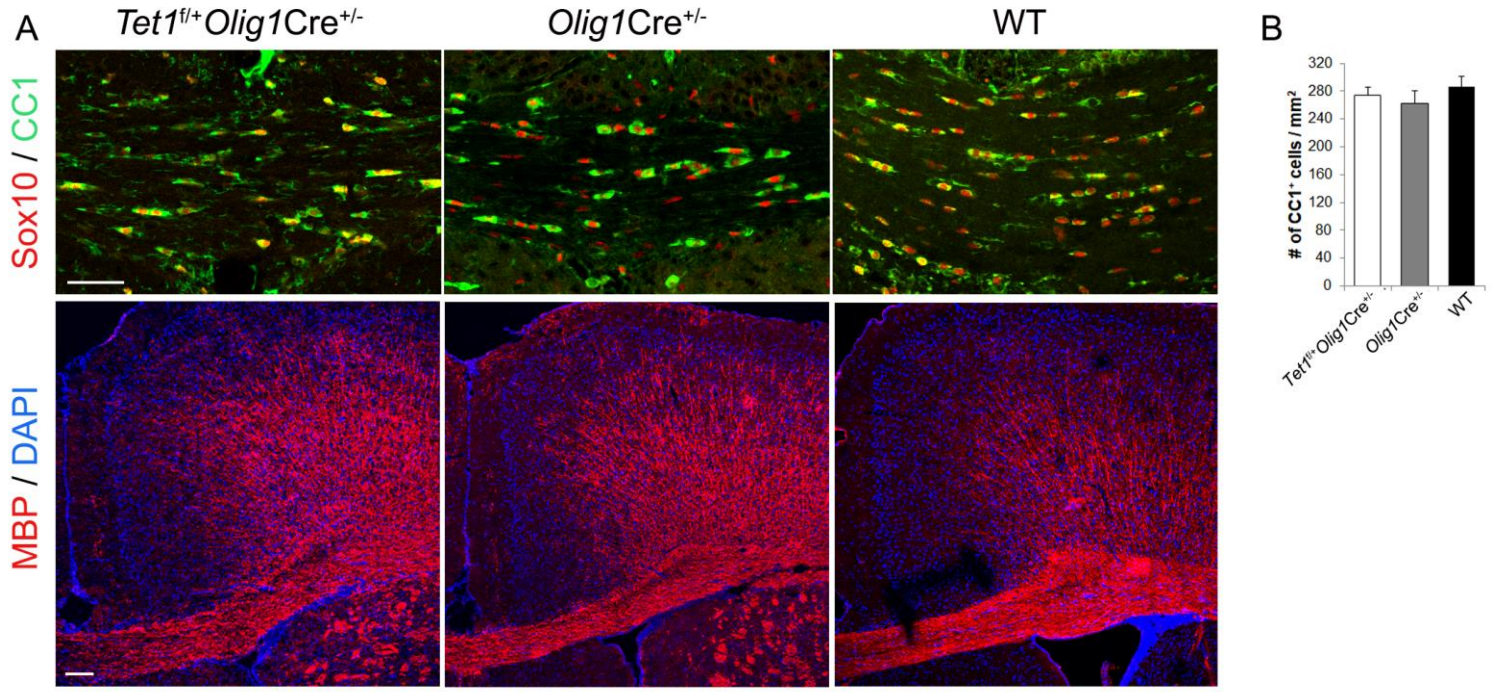
A
Tet1f/+Olig1Cre+/-
Olig1Cre+/-
WT
Sox10 / CC1
MBP / DAPI
B
# of CC1+ cells / mm2
320
280
240
200
160
120
80
40
0
Tet1f/+Olig1Cre+/-
Olig1Cre+/-
WT

Figure S3

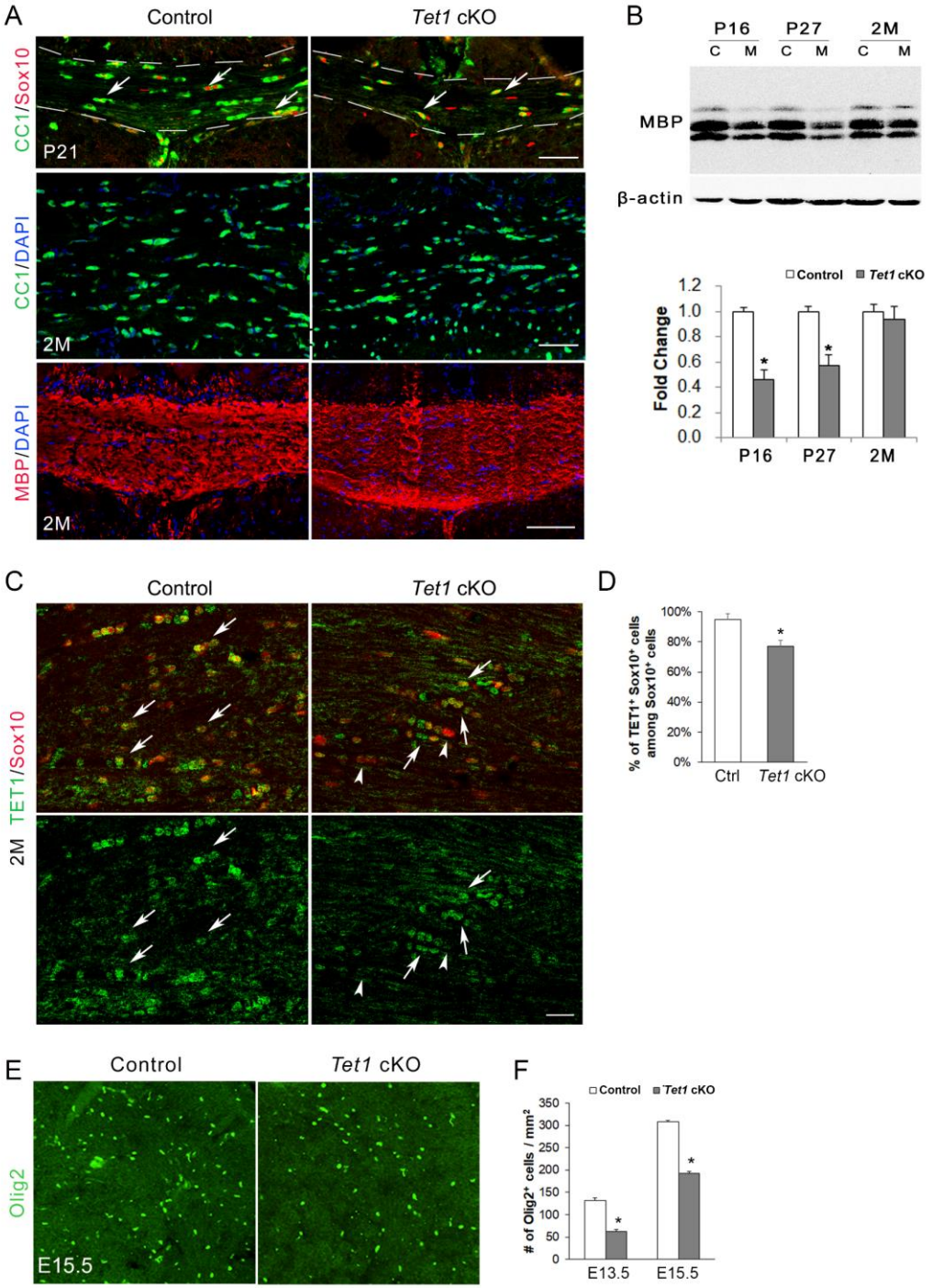
A
Control
Tet1 cKO
CC1/Sox10
P21
CC1/DAPI
2M
MBP/DAPI
2M
B
P16
P27
2M
C
M
C
M
C
M
MBP
β-actin
Control
Tet1 cKO
Fold Change
1.2
1.0
0.8
0.6
0.4
0.2
0.0
*
*
P16
P27
2M
C
Control
Tet1 cKO
2M
TET1/Sox10
D
% of TET1+ Sox10+ cells among Sox10+ cells
100%
80%
60%
40%
20%
0%
*
Ctrl
Tet1 cKO
E
Control
Tet1 cKO
Olig2
E15.5
F
Control
Tet1 cKO
# of Olig2+ cells / mm2
350
300
250
200
150
100
50
0
*
*
E13.5
E15.5

Figure S4

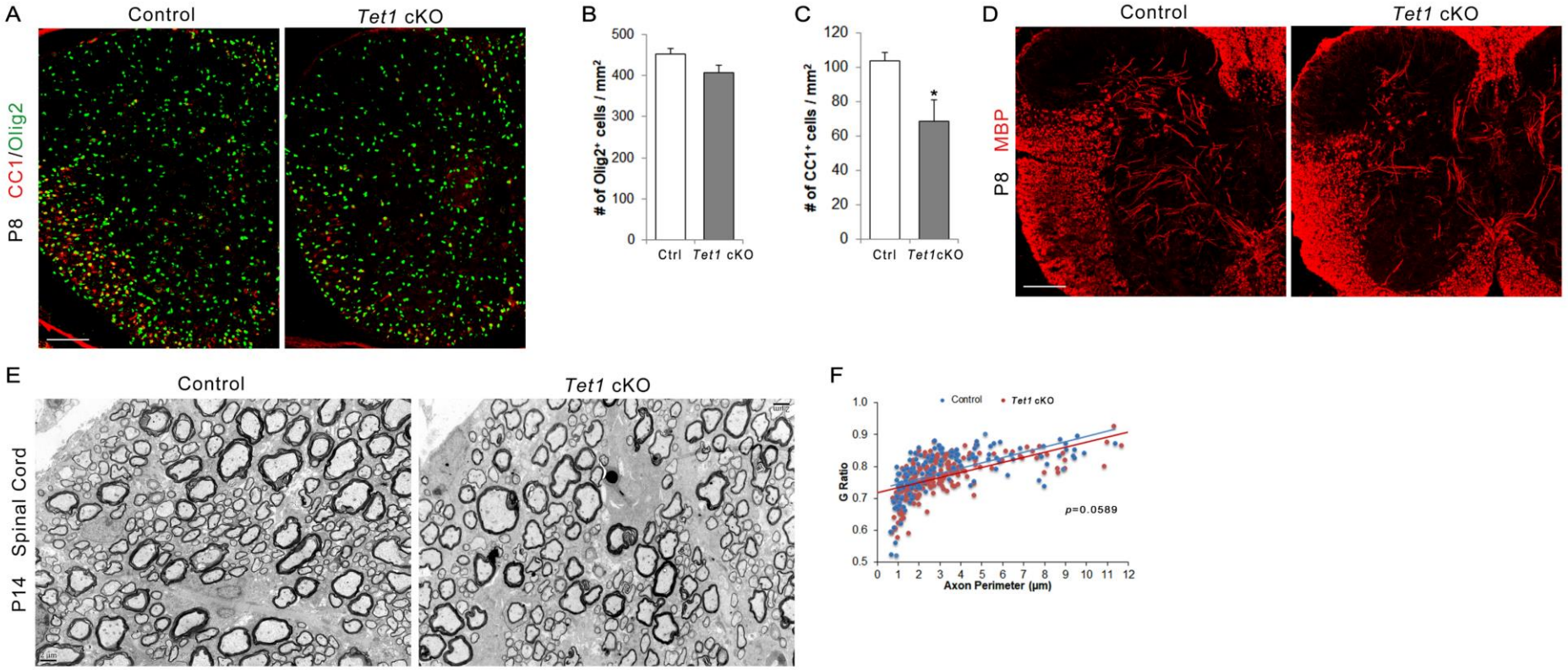
A
Control
Tet1 cKO
P8 CC1/Olig2
B
# of Olig2+ cells / mm2
500
400
300
200
100
0
Ctrl
Tet1 cKO
C
# of CC1+ cells / mm2
120
100
80
60
40
20
0
*
Ctrl
Tet1cKO
D
Control
Tet1 cKO
P8 MBP
E
Control
Tet1 cKO
P14 Spinal Cord
F
Control
Tet1 cKO
G Ratio
1.0
0.9
0.8
0.7
0.6
0.5
p=0.0589
0 1 2 3 4 5 6 7 8 9 10 11 12
Axon Perimeter (μm)

Figure S5

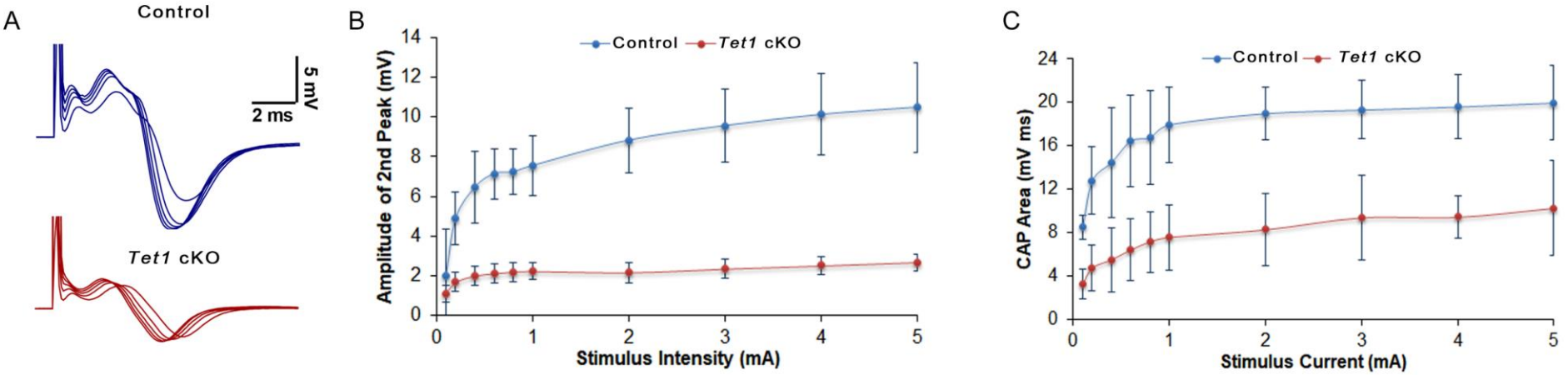
A
Control
5 mV
2 ms
Tet1 cKO
B
Control
Tet1 cKO
Amplitude of 2nd Peak (mV)
Stimulus Intensity (mA)
C
Control
Tet1 cKO
CAP Area (mV ms)
Stimulus Current (mA)

Figure S6

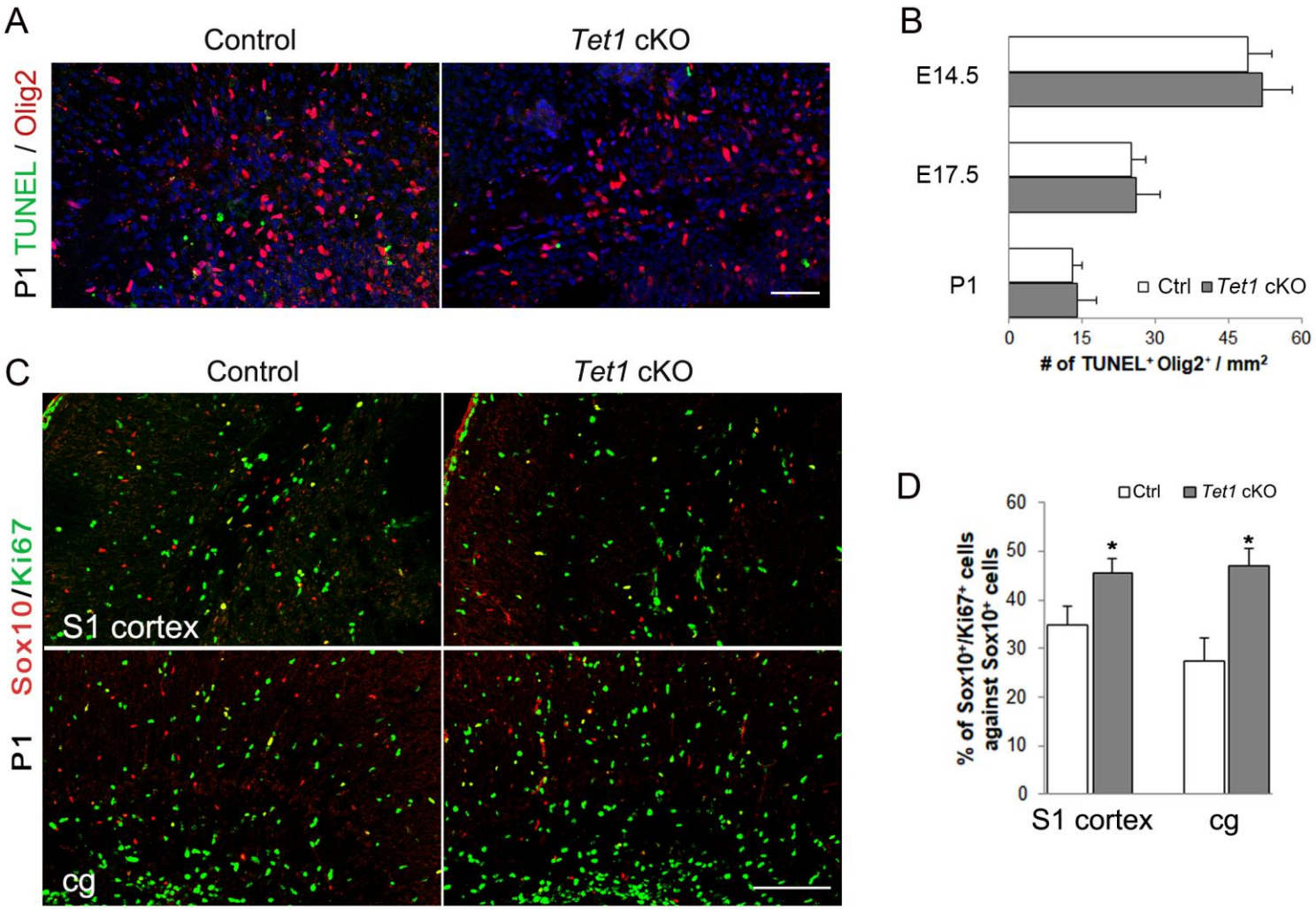
A
Control
Tet1 cKO
P1 TUNEL / Olig2
B
E14.5
E17.5
P1
Ctrl
Tet1 cKO
0
15
30
45
60
# of TUNEL+ Olig2+ / mm2
C
Control
Tet1 cKO
Sox10/Ki67
P1
S1 cortex
cg
D
Ctrl
Tet1 cKO
% of Sox10+/Ki67+ cells against Sox10+ cells
0
10
20
30
40
50
60
*
*
S1 cortex
cg

Figure S7

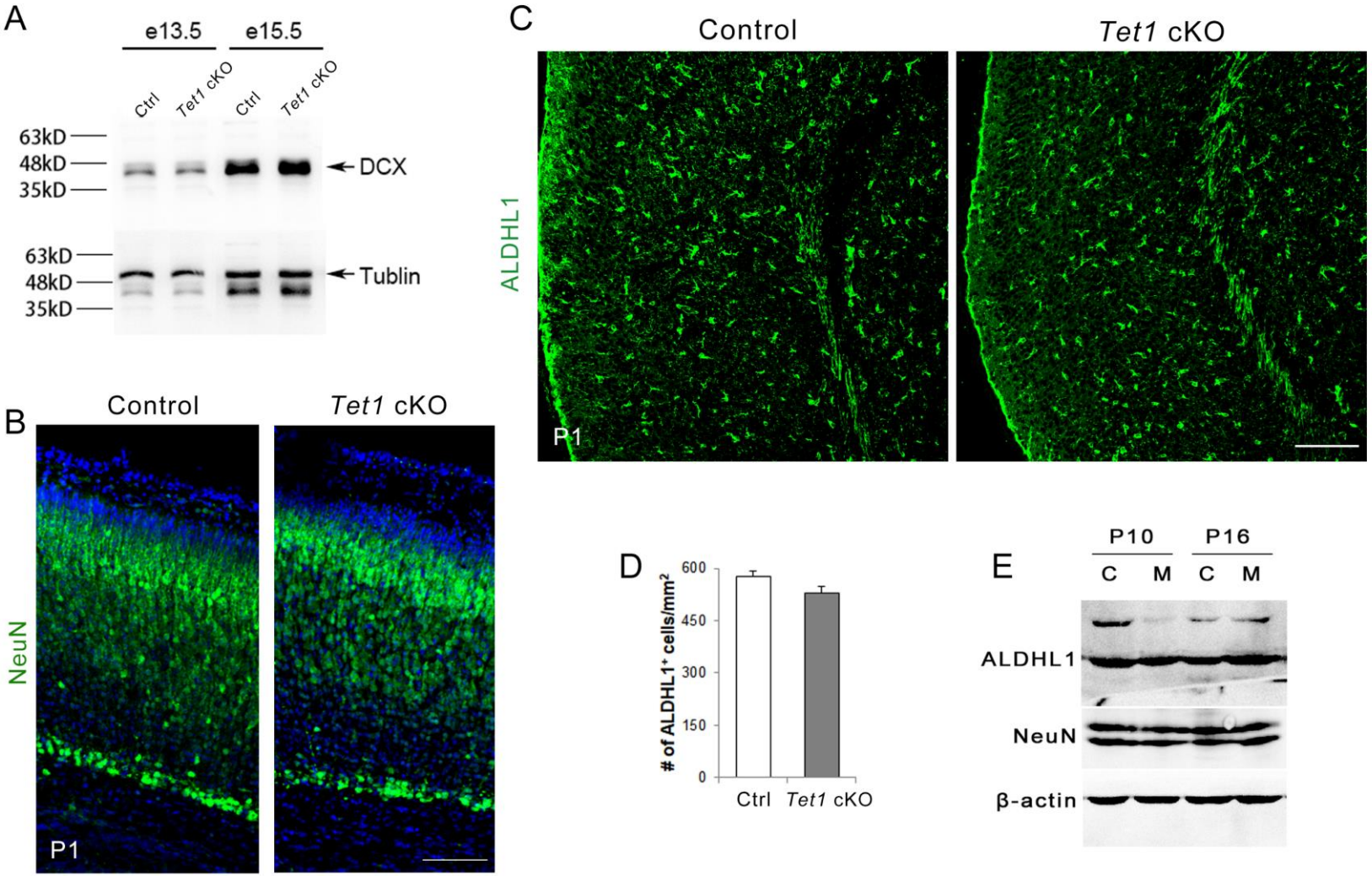
A
e13.5
e15.5
Ctrl
Tet1 cKO
Ctrl
Tet1 cKO
63kD
48kD
35kD
DCX
63kD
48kD
35kD
Tublin
B
Control
Tet1 cKO
NeuN
P1
C
Control
Tet1 cKO
ALDHL1
P1
D
# of ALDHL1+ cells/mm2
600
450
300
150
0
Ctrl
Tet1 cKO
E
P10
P16
C
M
C
M
ALDHL1
NeuN
β-actin

Figure S8

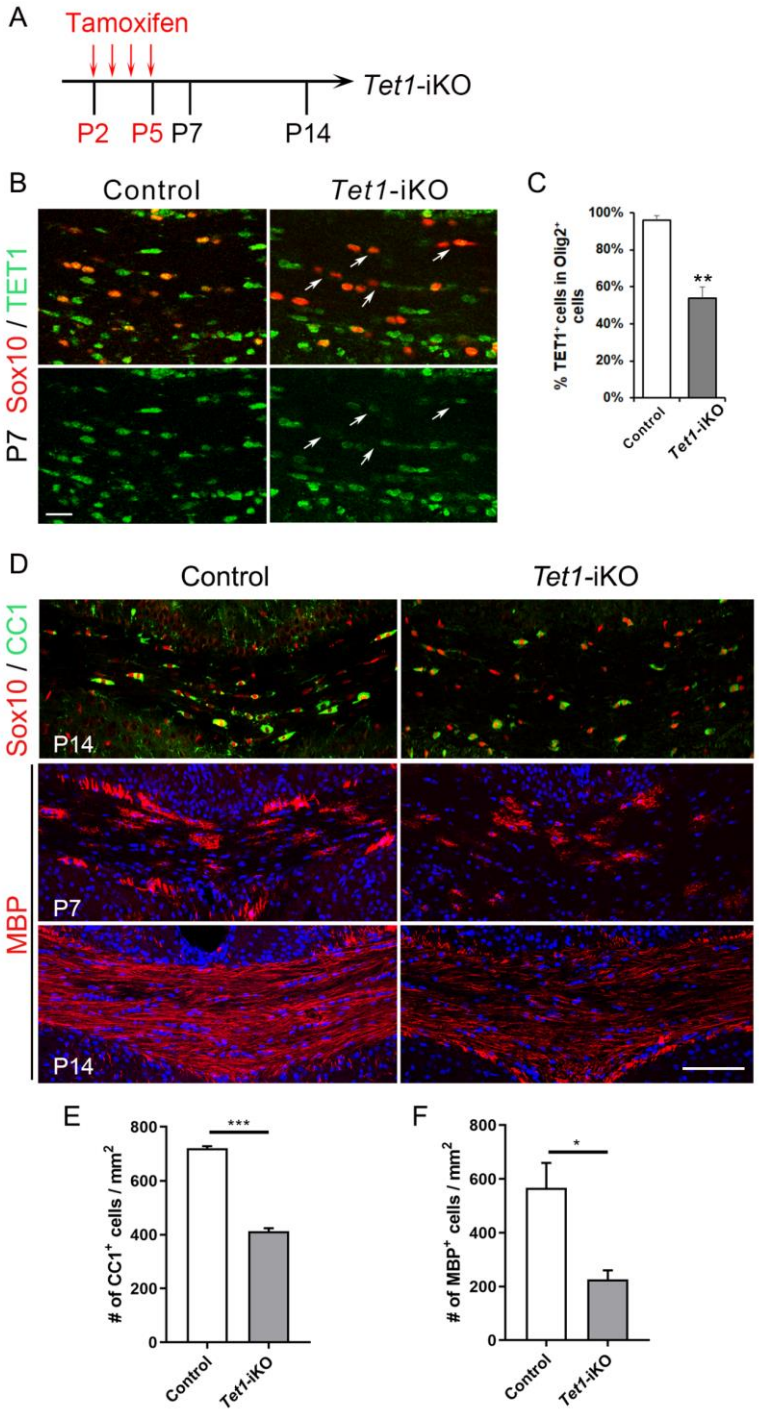
A
Tamoxifen
Tet1-iKO
P2
P5
P7
P14
B
Control
Tet1-iKO
Sox10 / TET1
P7
C
% TET1+ cells in Olig2+ cells
100%
80%
60%
40%
20%
0%
**
Control
Tet1-iKO
D
Control
Tet1-iKO
Sox10 / CC1
P14
MBP
P7
P14
E
# of CC1+ cells / mm2
800
600
400
200
0
***
Control
Tet1-iKO
F
# of MBP+ cells / mm2
800
600
400
200
0
*
Control
Tet1-iKO

Figure S9

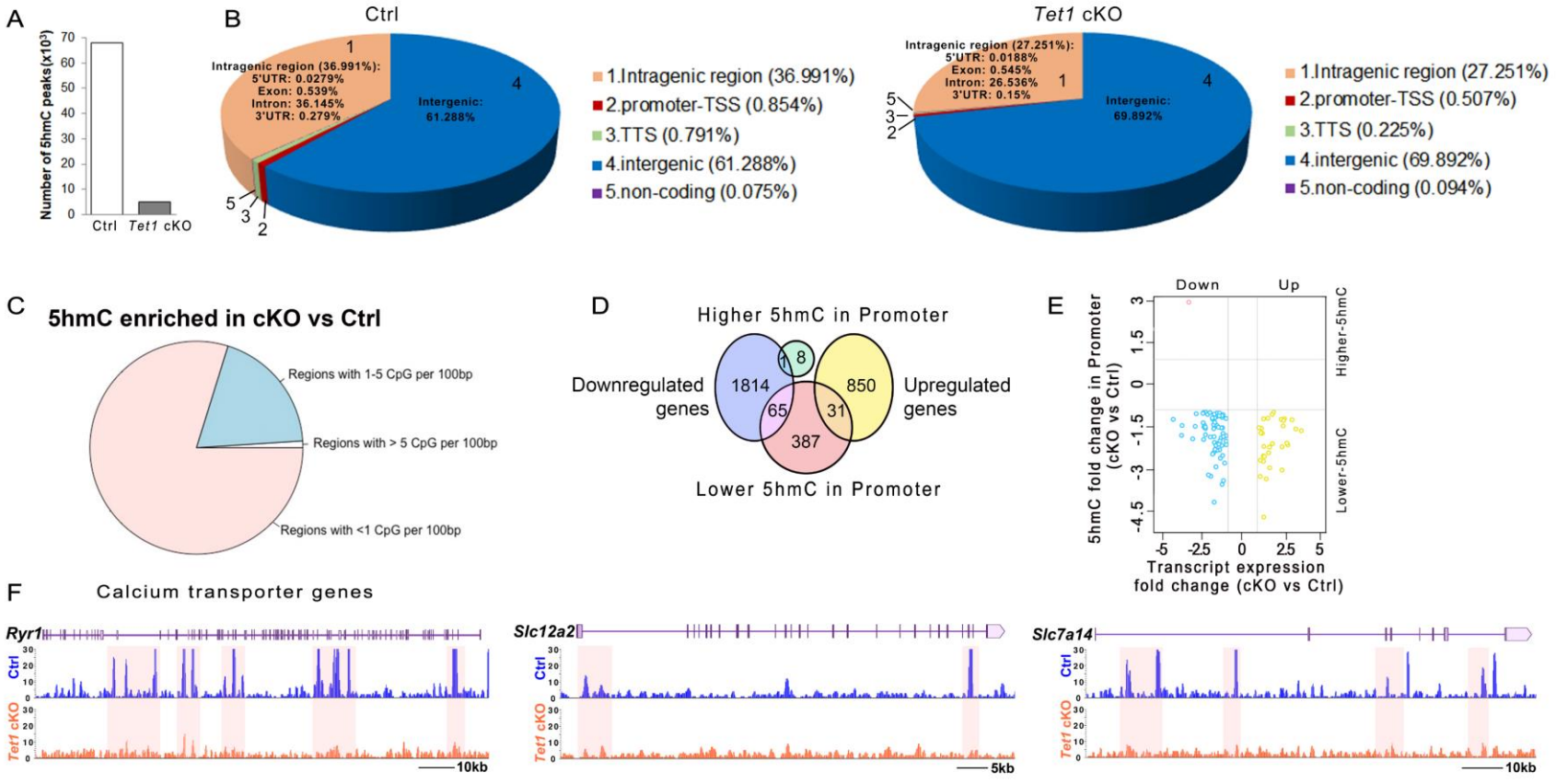
A
Number of 5hmC peaks (x10³)
70
60
50
40
30
20
10
0
Ctrl
Tet1 cKO
B
Ctrl
Intragenic region (36.991%):
5'UTR: 0.0279%
Exon: 0.539%
Intron: 36.145%
3'UTR: 0.279%
Intergenic:
61.288%
1
4
5
3
2
1.Intragenic region (36.991%)
2.promoter-TSS (0.854%)
3.TTS (0.791%)
4.intergenic (61.288%)
5.non-coding (0.075%)
Tet1 cKO
Intragenic region (27.251%):
5'UTR: 0.0188%
Exon: 0.545%
Intron: 26.536%
3'UTR: 0.15%
Intergenic:
69.892%
1
4
5
3
2
1.Intragenic region (27.251%)
2.promoter-TSS (0.507%)
3.TTS (0.225%)
4.intergenic (69.892%)
5.non-coding (0.094%)
C
5hmC enriched in cKO vs Ctrl
Regions with 1-5 CpG per 100bp
Regions with > 5 CpG per 100bp
Regions with <1 CpG per 100bp
D
Higher 5hmC in Promoter
Downregulated genes
Upregulated genes
Lower 5hmC in Promoter
1
8
1814
850
65
31
387
E
Down
Up
Higher-5hmC
Lower-5hmC
5hmC fold change in Promoter (cKO vs Ctrl)
3
1.5
0
-1.5
-3
-4.5
-5
-2.5
0
2.5
5
Transcript expression fold change (cKO vs Ctrl)
F
Calcium transporter genes
Ryr1
Slc12a2
Slc7a14
Ctrl
Tet1 cKO
10kb
5kb
10kb

Figure S10

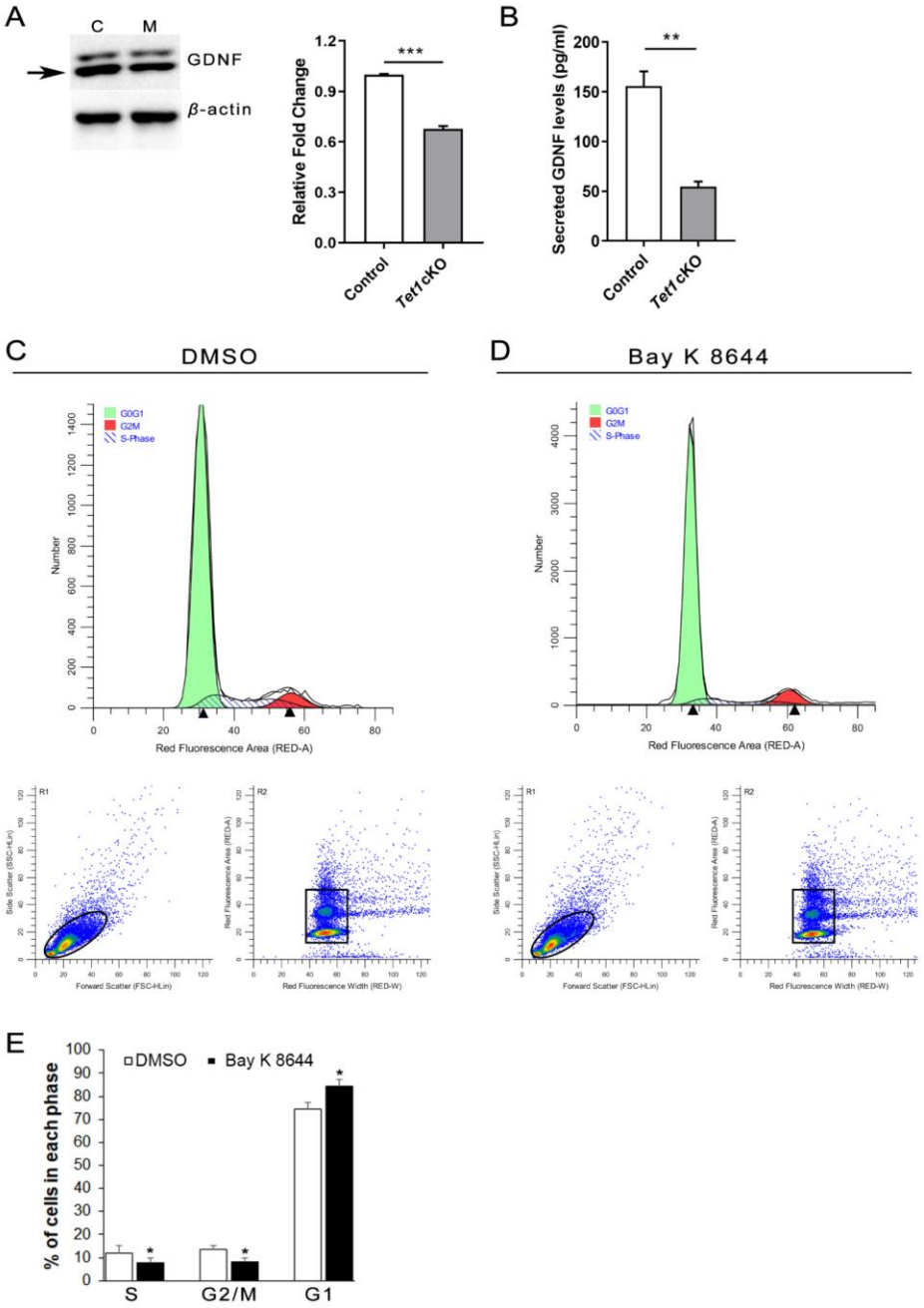
A
C
M
GDNF
β-actin
Relative Fold Change
1.2
0.9
0.6
0.3
0.0
***
Control
Tef1cKO
B
Secreted GDNF levels (pg/ml)
200
150
100
50
0
**
Control
Tef1cKO
C
DMSO
D
Bay K 8644
G0G1
G2M
S-Phase
Number
Red Fluorescence Area (RED-A)
R1
R2
Side Scatter (SSC-HLin)
Forward Scatter (FSC-HLin)
Red Fluorescence Area (RED-A)
Red Fluorescence Width (RED-W)
E
DMSO
Bay K 8644
% of cells in each phase
S
G2/M
G1

Figure S11

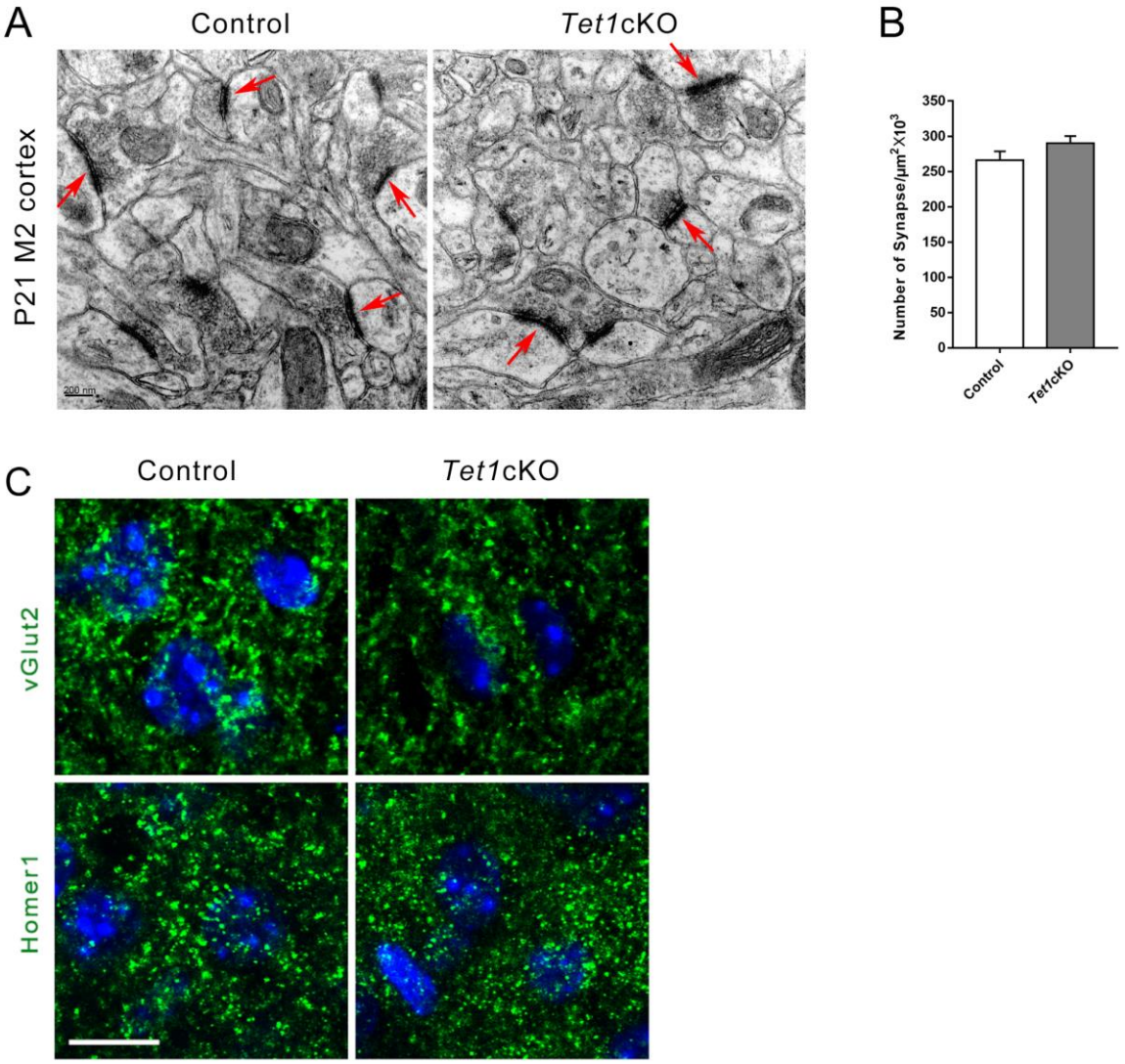
A
Control
Tet1cKO
P21 M2 cortex
200 nm
B
Number of Synapse/μm²X10³
350
300
250
200
150
100
50
0
Control
Tet1cKO
C
Control
Tet1cKO
vGlut2
Homer1

Figure S12